DG-GMsFEM for Problems in Perforated Domains with Non-Homogeneous Boundary Conditions

Valentin Alekseev [1,2,*], Maria Vasilyeva [3], Uygulaana Kalachikova [1] and **Eric T. Chung [4]**

[1] Multiscale Model Reduction Laboratory, North-Eastern Federal University, 677000 Yakutsk, Russia; lanasemna@mail.ru

[2] Yakutsk Branch of the Regional Scientific and Educational Mathematical Center "Far Eastern Center of Mathematical Research", North-Eastern Federal University, 677000 Yakutsk, Russia

[3] Center of Innovation for Flow through Porous Media, University of Wyoming, Laramie, WY 82071, USA; vasilyevadotmdotv@gmail.com

[4] Department of Mathematics, The Chinese University of Hong Kong, Shatin, New Territories, Hong Kong, China; tschung@math.cuhk.edu.hk

* Correspondence: alekseev.valen@mail.ru

Abstract: Problems in perforated media are complex and require high resolution grid construction to capture complex irregular perforation boundaries leading to the large discrete system of equations. In this paper, we develop a multiscale model reduction technique based on the Discontinuous Galerkin Generalized Multiscale Finite Element Method (DG-GMsFEM) for problems in perforated domains with non-homogeneous boundary conditions on perforations. This method implies division of the perforated domain into several non-overlapping subdomains constructing local multiscale basis functions for each. We use two types of multiscale basis functions, which are constructed by imposing suitable non-homogeneous boundary conditions on subdomain boundary and perforation boundary. The construction of these basis functions contains two steps: (1) snapshot space construction and (2) solution of local spectral problems for dimension reduction in the snapshot space. The presented method is used to solve different model problems: elliptic, parabolic, elastic, and thermoelastic equations with non-homogeneous boundary conditions on perforations. The concepts for coarse grid construction and definition of the local domains are presented and investigated numerically. Numerical results for two test cases with homogeneous and non-homogeneous boundary conditions are included, as well. For the case with homogeneous boundary conditions on perforations, results are shown using only local basis functions with non-homogeneous boundary condition on subdomain boundary and homogeneous boundary condition on perforation boundary. Both types of basis functions are needed in order to obtain accurate solutions, and they are shown for problems with non-homogeneous boundary conditions on perforations. The numerical results show that the proposed method provides good results with a significant reduction of the system size.

Keywords: multiscale method; discontinuous Galerkin; finite element method; perforated domain; non-homogeneous boundary condition; GMsFEM; multiscale model reduction; thermoelasticity problem

1. Introduction

Problems in perforated domains are of great interest additionally proposing many real-world applications. Take, for example, diffusion in perforated domains, mechanical processes in granular media, pore-scale flows in porous media, and so on [1–4]. Problems in perforated domains with non-homogeneous boundary conditions on perforations have great importance for a lot of applications in physics, biology, geology, and chemistry [5–8]. The main characteristic of perforated domains is the multiscale nature of the underlying processes. The solution techniques for these problems require high resolution in grid construction to capture complex irregular boundaries of perforations. Using direct numerical

methods to solve these problems is computationally challenging and expensive. In order to reduce the size of the system with accurate approximation, we use homogenization techniques and multiscale methods.

Reduction techniques are widely used today for problems in heterogeneous perforated media to reduce computational cost. In recent years, many methods have been developed focused on obtaining solutions on a coarse mesh. The homogenization method can be used for problems in perforated domains with scale separation [8–10]. For example, in Reference [11], the author considers the periodic homogenization problem in perforated domains that are formed by removing a periodic array of small holes from a fixed open bounded and connected domain with regular boundary. In the numerical homogenization method, the approximation of the solution on a coarse grid is constructed by calculating effective properties for coarse grid cells [12]. In Reference [13], the authors construct the machine learning methods for a fast calculation of effective characteristic for domains with random inclusions. In addition, for the perforated media without scale separation, the multiscale techniques are widely used [14,15]. Multiscale methods construct multiscale basis functions in each coarse-grid cell and couple these basis functions in a global formulation. Several studies have shown employment of multiscale methods as solution to problems in perforated domains [16–19]. There are also studies presenting the multiscale approach based on Crouzeix-Raviart coupling of multiscale finite element basis [16,17]. The generalization of the heterogeneous multiscale finite element method for elliptic problems in perforated domains is presented in work of Henning and Ohlberger (2009) [18]. In order to avoid a limited number of degrees of freedom per coarse element, this paper considers the Generalized Multiscale Finite Element Method (GMsFEM) for solution problems in perforated domains [19–22]. The GMsFEM is a general multiscale procedure, wherein the model reduction is based on some local multiscale basis functions that are constructed using local spectral decomposition. In our earlier study [19], we presented an accurate multiscale approximation using GMsFEM with several basis functions in each local domain. The problems with non-homogeneous boundary conditions on perforations are studied in References [23,24], where authors evaluate construction of the additional basis functions for perforation boundary. The multiscale model reduction technique, based on Discontinuous Galerkin Generalized Multiscale Finite Element Method (DG-GMsFEM), is presented in Reference [22], where we consider the solution of the problems with homogeneous boundary conditions. Additional points of multiscale methods can distinguish methods, such as upscaling method using non-local multicontinuum method (NLMC) [24,25], which can be effective for heterogeneous. The main part of the method is the construction of suitable local basis functions with the capability of capturing multiscale features and non-local effects. Another method that deserves attention is the constraint energy minimizing generalized multiscale finite element method (CEM-GMsFEM) [26,27]. The main purpose of this method is that the convergence of the method is independent of contrast and decreases linearly with respect to the cell size if the oversampling size is chosen appropriately. In addition, for punctured tasks, the oversampling method can be especially useful and improve accuracy and convergence [28–30]. Besides, the oversampling strategy is used to reduce the mismatching effects of boundary conditions imposed artificially in the construction of snapshot basis functions.

This paper presents an extension of the DG-GMsFEM for problems with non-homogeneous boundary conditions on perforations. The presented approach is based on the construction of a separate multiscale space for coarse cell interfaces and for local perforation boundary. We present a unified approach for different types of problems: elliptic, parabolic, elastic, and thermoelastic problems. Using the DG-GMsFEM for coarse grid coupling, we construct multiscale basis functions to generate an accurate lower-dimensional model on a coarse grid. The paper starts with the construction of the snapshot space that contains a set of local solutions in each coarse cell with various boundary conditions. In order to perform a dimension reduction of the snapshot space and define multiscale basis functions, we solve a local spectral problem in the snapshot space. The construction of

two types of multiscale basis functions for subdomain boundary and perforation boundary are presented separately. The presented perforation boundary basis functions are used to approximate non-homogeneous boundary conditions on perforations. The numerical results for two-dimensional problems with homogeneous and non-homogeneous boundary conditions on perforations are presented. We investigate a different number of subdomain and perforation boundary multiscale basis functions and show that an accurate solution can be obtained with a large reduction of the system size with a sufficient number of multiscale basis functions. The coarse grid construction and definition of the local domains are presented and investigated numerically for each of the considered equations.

This paper is organized as follows. Section 2 contains description of the problem formulation. The fine-scale approximation using the interior penalty discontinuous Galerkin (IPDG) method is given in Section 3. The multiscale method based on DG-GMsFEM is presented in Section 4 with the description of the construction of the multiscale basis functions. Section 5 presents numerical results for the two-dimensional problem in a perforated domain with homogeneous and non-homogeneous boundary conditions on perforations. Results are shown for the different number of multiscale basis functions, as well as results for different types of problems (elliptic, parabolic, elastic, and thermoelastic). The results for quasi-structured and unstructured coarse grid are presented. Finally, the conclusion is given in Section 6.

2. Problem Formulation

Let Ω be a perforated domain and Γ_p be the perforation boundary. In this work, we consider the elliptic equation in perforated domain

$$\mathcal{L}(u) = f, \quad x \in \Omega, \tag{1}$$

with

$$u = g_g, \quad x \in \Gamma_g, \tag{2}$$

and non-homogeneous boundary conditions on perforation boundary

$$\mathcal{B}(u) = \alpha u + g_p, \quad x \in \Gamma_p, \tag{3}$$

where f is a given source vector, $\mathcal{L}$ denotes a linear differential operator, $\mathcal{B}$ is a normal derivative operator, and $\partial\Omega = \Gamma_g \cup \Gamma_p$.

- For the Laplace operator, we have

$$\mathcal{L}(u) = \nabla \cdot q(u), \quad \mathcal{B}(u) = q \cdot n, \tag{4}$$

  with

$$q(u) = -k\nabla u,$$

  where $q(u)$ is the flux, k is the diffusion coefficient, and n is the outward unit normal on $\partial\Omega$.

- For the elasticity operator, we have

$$\mathcal{L}(u) = \nabla \cdot \sigma(u), \quad \mathcal{B}(u) = \sigma \cdot n, \tag{5}$$

  with

$$\sigma(u) = 2\mu\varepsilon(u) + \lambda \nabla \cdot u \, \mathcal{I}, \quad \varepsilon(u) = \frac{1}{2}(\nabla u + \nabla u^{Tr}),$$

  where u is the displacement field, $\varepsilon(u)$ is the strain tensor, $\sigma(u)$ is the stress tensor, u^{Tr} is the transpose of u, and λ and μ are the Lamé coefficients.

3. Fine-Grid Approximation

This section shows an approximation using the interior penalty discontinuous Galerkin method (IPDG) on the fine grid that resolves all perforations on the grid level.

Let $\mathcal{T}^h$ be a fine-grid partition of the domain Ω given by

$$\mathcal{T}^h = \bigcup_{i=1}^{N_{cell}^h} K_i,$$

where N_{cell}^h is the number of fine grid cells. We use $\mathcal{E}^h$ to denote the set of facets in $\mathcal{T}^h$ with $\mathcal{E}^h = \mathcal{E}_o^h \cup \mathcal{E}_b^h$, where $\mathcal{E}_o^h$ and $\mathcal{E}_b^h$ are the set of interior and boundary facets (see Figure 1).
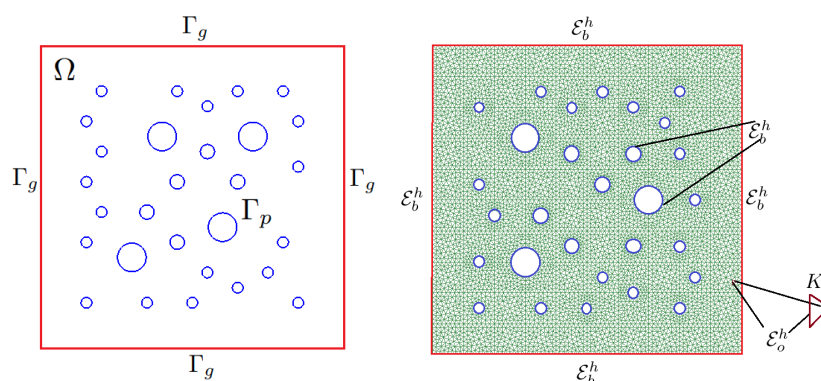

Figure 1. Illustration of perforated domain Ω (**left**) and fine grid $\mathcal{T}^h$ (**right**).

Defining the jump $[u]$ and the average $\{u\}$ of a function u on the interior facet by

$$[u] = u_+ - u_-, \quad \{u\} = \frac{u_+ + u_-}{2},$$

where $u_+ = u|_{K^+}$, $u_- = u|_{K^-}$, and K^+ and K^- are the two cells sharing the facet E. For boundary facets, we have $[u] = u|_E$ and $\{u\} = u|_E$, $E \in \mathcal{E}_b^h$.

For IPDG approximation, the following variational formulation of the problem is used: find $u_h \in V_h$ such that

$$a(u_h, v) = l(v), \quad \forall v \in V_h, \tag{6}$$

where:

- for the Laplace operator, we have $V_h = \{v \in L^2(\Omega) : v|_K \in \mathbb{P}_1(K), \forall K \in \mathcal{T}^h\}$ and

$$a(u, v) = \sum_{K \in \mathcal{T}^h} \int_K (k \nabla u, \nabla v) \, dx + \sum_{E \in \mathcal{E}_{b,p}^h} \int_E \alpha \, u \, v \, ds$$

$$- \sum_{E \in \mathcal{E}_o^h \cup \mathcal{E}_{b,g}^h} \int_E \left(\{k \nabla u \cdot n\} \cdot [v] + \{k \nabla v \cdot n\} \cdot [u] - \frac{\gamma_f}{h} \{k\} [u] \cdot [v] \right) ds,$$

$$l(v) = \sum_{K \in \mathcal{T}^h} \int_K f \, v \, dx + \sum_{E \in \mathcal{E}_{b,p}^h} \int_E g_p \, v \, ds$$

$$+ \sum_{E \in \mathcal{E}_{b,g}^h} \int_E \left(\frac{\gamma_f}{h} k \, v - k \nabla v \cdot n \right) g_g \, ds.$$

- for the elasticity operator, we have $V_h = \{v \in [L^2(\Omega)]^2 : v|_K \in [\mathbb{P}_1(K)]^2, \forall K \in \mathcal{T}^h\}$, and

$$a(u,v) = \sum_{K \in \mathcal{T}^h} \int_K (\sigma(u), \varepsilon(v)) dx + \sum_{E \in \mathcal{E}^h_{b,p}} \int_E \alpha\, u\, v\, ds$$

$$- \sum_{E \in \mathcal{E}^h_o \cup \mathcal{E}^h_{b,g}} \int_E \left(\{\tau(u)\}[v] + \{\tau(v)\}[u] - \frac{\gamma_f}{h}\{\lambda + 2\mu\}[u][v] \right) ds,$$

$$l(v) = \sum_{K \in \mathcal{T}^h} \int_K f \cdot v\, dx + \sum_{E \in \mathcal{E}^h_{b,p}} \int_E g_p \cdot v\, ds$$

$$+ \sum_{E \in \mathcal{E}^h_{b,g}} \int_E \left(\frac{\gamma_f}{h}(\lambda + 2\mu)\, v - \tau(v) \right) \cdot g_g\, ds$$

where $\tau(u) = \sigma(u) \cdot n$.

Here, γ_f is the penalty parameter.

The above systems can be written in the matrix form as follows:

$$A_h U_h = F_h,$$

where

$$A_h = [a_{i,j}], \quad a_{i,j} = a(\varphi_i, \varphi_j), \quad F_h = [f_j], \quad f_j = l(\varphi_j),$$

with $u_h = \sum_i u_i \varphi_i$ and $U_h = [u_j]$.

4. Multiscale Method

This section describes the construction of multiscale approximation on the coarse grid using the Discontinuous Galerkin Generalized Multiscale Finite Element method (DG-GMsFEM) [22,31,32].

Let $\mathcal{T}^H$ be a coarse-grid partition of the domain Ω with coarse mesh size H (see Figure 2).

$$\mathcal{T}^H = \bigcup_{i=1}^{N^H_{cell}} K_i,$$

where N^H_{cell} is the number of coarse grid cells, and K_i is coarse cell (local domain). Use $\mathcal{E}^H$ to denote the set of facets in $\mathcal{T}^H$ with $\mathcal{E}^H = \mathcal{E}^H_o \cup \mathcal{E}^H_b$. Note that, in DG-GMsFEM, the multiscale basis functions are supported in each coarse cell K_i.
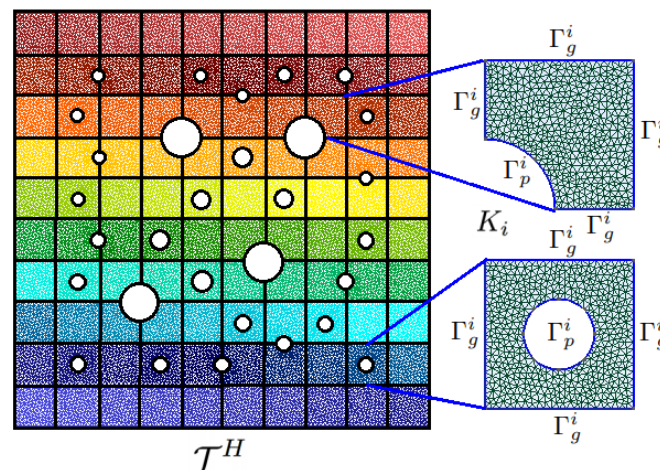

Figure 2. Coarse grid $\mathcal{T}^H$ with coarse cell K_i, $\Gamma^i_g \cup \Gamma^i_p = \partial K_i$.

Defining V_H as the multiscale space

$$V_H = \text{span}\{\phi_i\}_{i=1}^{N_u},$$

parabolic, elastic, and thermoelastic $N_u = \dim(V_H)$ is the number of basis functions.

For the coarse grid approximation, we use a DG approach and have the following variational formulation: find $u_H \in V_H$ such that

$$a(u_H, v) = l(v), \quad \forall v \in V_H. \tag{7}$$

Note that the coarse-scale system can be formed by projecting the fine-scale system onto the coarse grid. The projection matrix can be assembled using the multiscale basis functions.

To construct the multiscale space, we start with the construction of the snapshot space that contains a set of basis functions formed by the solution of local problems with all possible boundary conditions up to the fine grid resolution in each coarse cell K_i (local domain) for $i = 1, \cdots, N$, parabolic, elastic, and thermoelastic N is the number of coarse blocks in Ω. After that, we solve a spectral problem to select dominant modes of the snapshot space.

Next, we present the details of constructing the multiscale basis functions considering two types of basis functions related to the two boundaries: (1) subdomain boundaries Γ_g^i and (2) perforation boundary Γ_p^i.

Subdomain boundary muliscale basis functions. In the local snapshot space consisting of functions u_l^i, which are solutions to the following local problem

$$\mathcal{L}(u_l^i) = 0, \quad x \in K_i, \tag{8}$$

with the following boundary condition on subdomain boundaries,

$$u_l^i = g_i^l, \quad x \in \Gamma_g^i,$$

and, on perforation boundary, we set homogeneous boundary condition related to (3)

$$\mathcal{B}(u_l^i) = \alpha u_l^i, \quad x \in \Gamma_p^i,$$

where $l = 1, \cdots, L_i^g$. Local problems are solved using IPDG approximation on fine mesh $\mathcal{T}^h(K_i)$. For Laplace operator, we have $L_i^g = J_i^g$ local problems, where J_i^g is the number of fine grid facets on Γ_g^i, and $g_i^l = \delta_i^l$ is the Kronecker delta function that has value 1 if $i = l$ and value 0 else. For elasticity operator, we have $L_i^g = d \cdot J_i^g$ local problems, where d is the dimension, and $g_i^l = (\delta_i^l, 0)$ and $(0, \delta_i^l)$ for $d = 2$.

The collection of the solutions of the above local problems generates the snapshot space in the local domain K_i

$$V_g^{i,\text{snap}} = \{u_l^i : 1 \le l \le L_i^g\}, \quad R_g^{i,\text{snap}} = \left[u_1^i, \ldots, u_{L_i^g}^i \right]^{Tr}.$$

To reduce the size of the snapshot space, we solve the following local spectral problem in the snapshot space $V_g^{i,\text{snap}}$

$$\tilde{A}_g^{K_i} \tilde{\psi}_g^i = \lambda_o \tilde{S}_g^{K_i} \tilde{\psi}_g^i, \tag{9}$$

where

$$\tilde{A}_g^{K_i} = R_g^{i,\text{snap}} A_h^{K_i} (R_g^{i,\text{snap}})^{Tr}, \quad \tilde{S}_g^{K_i} = R_g^{i,\text{snap}} S_h^{K_i} (R_g^{i,\text{snap}})^{Tr}.$$

Here, $A_h^{K_i}$ and $S_h^{K_i}$ are the matrix representation of the bilinear forms $a^{K_i}(u, v)$ and $s^{K_i}(u, v)$

- For Laplace operator:

$$a^{K_i}(u,v) = \sum_{K \in \mathcal{T}^h(K_i)} \int_K k \nabla u \cdot \nabla v \, dx$$

$$- \sum_{E \in \mathcal{E}_o^h(K_i)} \int_E \left(\{k \nabla u \cdot n\} \cdot [v] + \{k \nabla v \cdot n\} \cdot [u] - \frac{\gamma_f}{h} \{k\} [u] \cdot [v] \right) ds, \quad (10)$$

$$s^{K_i}(u,v) = \sum_{E \in \mathcal{E}_b^h(K_i)} \int_E k \, u \, v \, ds.$$

- For elasticity operator:

$$a^{K_i}(u,v) = \sum_{K \in \mathcal{T}^h(K_i)} \int_K (\sigma(u), \varepsilon(v)) dx$$

$$- \sum_{E \in \mathcal{E}_o^h(K_i)} \int_E \left(\{\tau(u)\}[v] + \{\tau(v)\}[u] - \frac{\gamma_f}{h} \{\lambda + 2\mu\}[u][v] \right) ds, \quad (11)$$

$$s^{u,K_i}(u,v) = \sum_{E \in \mathcal{E}_b^h(K_i)} \int_E (\lambda + 2\mu) u \cdot v \, ds.$$

It should be noted that the integral in $s^{K_i}(u,v)$ is defined on the boundary of the coarse block K_i and based on the definition of the snapshot space used to extract dominant modes related to the outer boundary of the local domain.

Next, we arrange the eigenvalues in increasing order and choose the first eigenvectors corresponding to the first smallest eigenvalues $\psi_{g,k}^i = (R_g^{i,\text{snap}})^{Tr} \tilde{\psi}_{g,k}^i$ as the basis functions $(k = 1, \ldots, M_g^i)$

$$V_H^g = \text{span}\{\psi_{g,k}^i : 1 \le i \le N_{cell}^H, 1 \le k \le M_g^i\}.$$

The first five eigenvectors for some local domains K_i are depicted in Figure 3 for Laplace operator and in Figure 4 for elasticity operator.

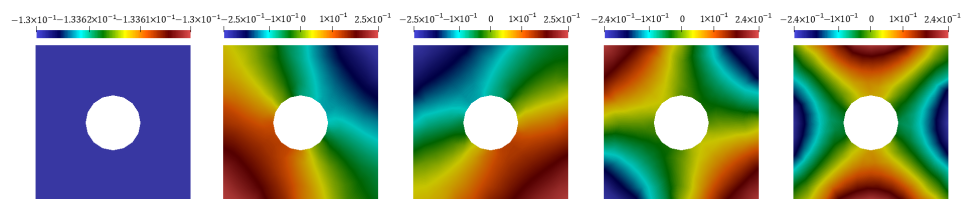**Figure 3.** Illustration of the outer boundary multiscale basis functions for Laplace problem, $\psi_{g,k}^i$ for $k = 1, \ldots, 5$ (from **left** to **right**).
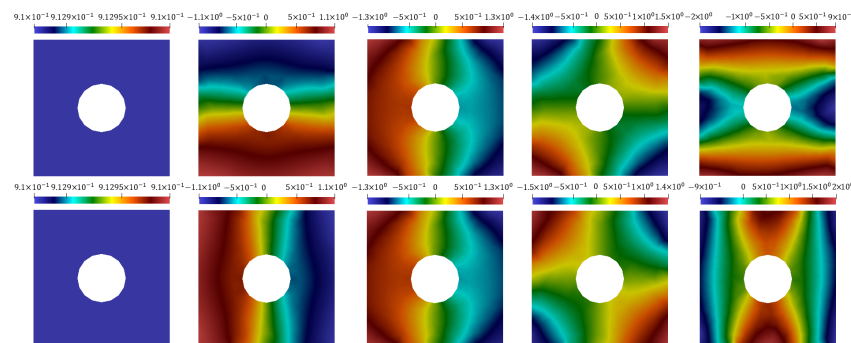

Figure 4. Illustration of the outer boundary multiscale basis functions for elasticity problem, $\psi_{g,k}^i$ for $k = 1, \ldots, 5$ (from **left** to **right**). First row: displacement X-component. Second row: displacement Y-component.

Perforation boundary muliscale basis functions. To handle non-homogeneous boundary conditions on the perforation boundaries, we construct an additional multiscale basis functions. The snapshot space is constructed by solution of the following problem in local domain K^i that contains perforations

$$\mathcal{L}(u_l^i) = 0, \quad x \in K_i,　\tag{12}$$

with the homogeneous boundary condition on subdomain boundaries,

$$u_l^i = 0, \quad x \in \Gamma_g^i,$$

and, on the perforation boundary, we set the following boundary condition related to (3)

$$\mathcal{B}(u_l^i) = \alpha u_l^i + g_i^l, \quad x \in \Gamma_p^i,$$

where $l = 1, \cdots, L_i^p$, where $L_i^p = J_i^p$ for Laplace problem, and $L_i^p = d \cdot J_i^p$ for elasticity problem (J_i^p is the number of fine grid facets on Γ_p^i).

We form a snapshot space using local solutions

$$V_p^{i,\text{snap}} = \{u_l^i : 1 \le l \le L_i^p\}, \quad R_p^{i,\text{snap}} = \left[u_1^i, \dots, u_{L_i^p}^i \right]^{Tr}.$$

We perform a dimension reduction in the snapshot space using the local spectralproblem

$$\tilde{A}_p^{K_i} \tilde{\psi}_{g,k}^i = \eta \tilde{S}_p^{K_i} \tilde{\psi}_{g,k}^i,　\tag{13}$$

where

$$\tilde{A}_p^{K_i} = R_p^{i,\text{snap}} A_h^{K_i} (R_p^{i,\text{snap}})^{Tr}, \quad \tilde{S}_p^{K_i} = R_p^{i,\text{snap}} S_h^{K_i} (R_p^{i,\text{snap}})^{Tr}.$$

The eigenvalues are arranged in increasing order, and, by choosing the first eigenvectors corresponding to the first smallest eigenvalues, we define perforation boundary multiscale basis functions

$$V_H^p = \text{span}\{\psi_{g,k}^i : 1 \le i \le N_{cell,p}^H, 2 \le k \le M_p^i\},$$

where $\psi_{g,k}^i = (R_p^{i,\text{snap}})^{Tr} \tilde{\psi}_{g,k}^i$ for $k = 1, \dots, M_p^i$, and $N_{cell,p}$ is the number of local domains with perforations. It should be noted that the first eigenvector was not taken because constant valued vector already exists in outer boundary multiscale space. The perforation boundary of multiscale basis functions are presented in Figure 5 for Laplace problem and in Figure 6 for elasticity problem.
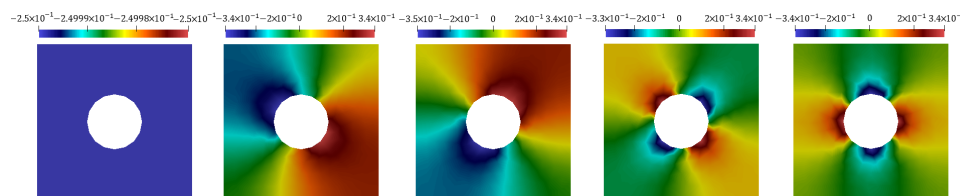

Figure 5. Illustration of the perforation boundary multiscale basis functions for Laplace problem, $\psi_{p,k}^i$ for $k = 1, \dots, 5$ (from **left** to **right**).
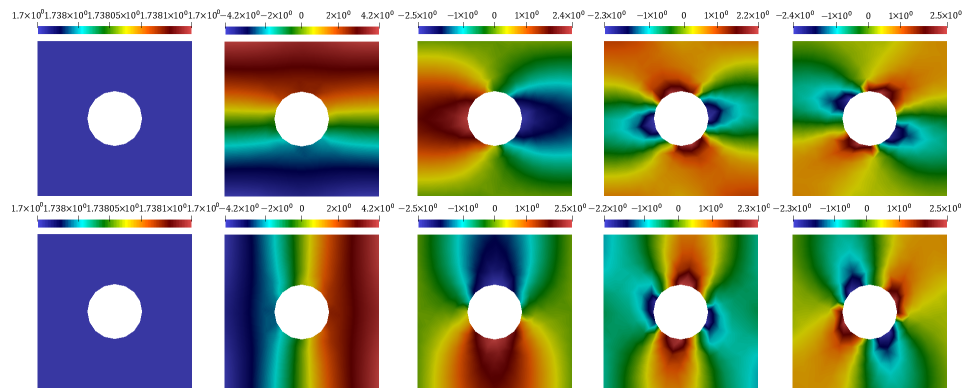
Figure 6. Illustration of the perforation boundary multiscale basis functions for elasticity problem, $\psi_{p,k}^i$ for $k = 1, \ldots, 5$ (from **left** to **right**). First row: displacement X - component. Second row: displacement Y-component.

Interior multiscale basis functions. We add one interior basis functions [22,32] constructed by solution of the following local problem:

$$\mathcal{L}(\phi^i) = f, \quad x \in K_i, \tag{14}$$

with $f = 1$ and homogeneous boundary condition on subdomain and perforation boundaries,

$$\phi^i = 0, \quad x \in \Gamma_g^i, \quad \mathcal{B}(\phi) = \alpha\phi, \quad x \in \Gamma_p^i.$$

Finally, there is the following multiscale space:

$$V_H = \mathrm{span}\{\psi_{g,k}^i, \psi_{p,m}^j, \phi^i : 1 \leq i \leq N_g, 1 \leq j \leq N_p, 1 \leq k \leq M_g^i, 2 \leq m \leq M_p^i\},$$

where $N_p = N_{cell,p}$, and $N_g = N_{cell}$

Coarse scale system. To construct the coarse grid system, we generate a projection matrix using multiscale basis functions

$$R = \left[\psi_{g,1}^1, \ldots, \psi_{g,M_g^{N_g}}^{N_g}, \psi_{p,1}^2, \ldots, \psi_{p,M_p^{N_p}}^{N_p}, \phi_1, \ldots, \phi_{N_{cell}^H}\right]^{Tr}.$$

Using projection matrix, we have the following coarse grid system in matrix form:

$$A_H U_H = F_H, \tag{15}$$

where

$$A_H = R A_h R^{Tr}, \quad F_H = R F_h.$$

After the solution of the coarse-scale system, the fine-scale solution for displacement can be recovered $U_{ms} = R^{Tr} U_H$.

5. Numerical Results

We present numerical results for the model problems in the perforated domain $\Omega = [0, L_x] \times [0, L_y]$ with $L_x = L_y = 1$. The computational domain with coarse and fine grids is presented in Figure 7. The fine grid contains 14,648 vertices and 28,410 cells. The coarse grid contains 121 vertices and 100 cells (local domains). To construct the computational domain with computational mesh, we use the mesh generator Gmsh [33].
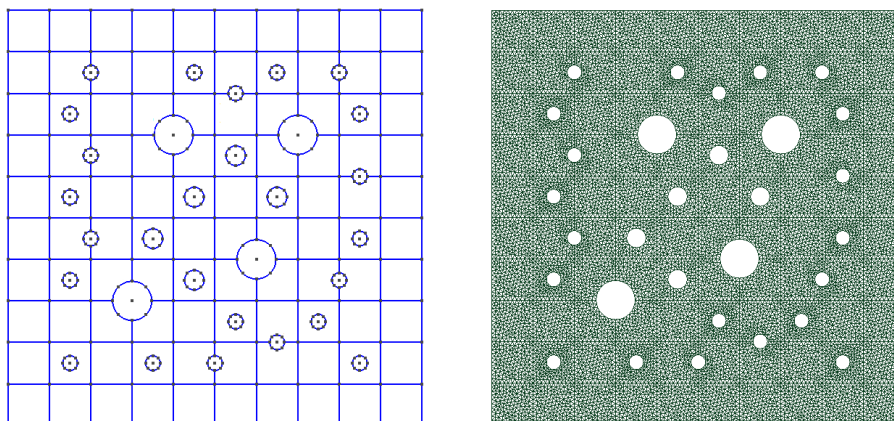
Figure 7. Computational domain with coarse (**left**) and fine (**right**) grids.

To investigate the presented multiscale method for problems solving in perforated domains, the following tests are considered: (1) elliptic equation and (2) elasticity equation. The extension of the method for solution of the parabolic and thermoelasticity problems are presented in Appendixes A and B . The numerical implementation of the model problems is based on the FEniCS computing platform [34]. There are two test cases for each problem:

- *Case 1.* homogeneous boundary conditions on perforations;
- *Case 2.* non-homogeneous boundary conditions on perforations.

We calculate the following relative errors in L^2 and energy norm (semi-norm H^1) between multiscale and fine-grid solution:

$$e_{L^2} = \sqrt{\frac{\int_\Omega (u_{ms} - u)^2 \, dx}{\int_\Omega u^2 \, dx}} \cdot 100\%, \quad e_{H^1} = \sqrt{\frac{\int_\Omega a(u_{ms} - u, u_{ms} - u) \, dx}{\int_\Omega a(u, u) \, dx}} \cdot 100\%,$$

where u and u_{ms} are the fine-scale and multiscale solutions, respectively.

To start, there are results for elliptic and elastic equations. Whereat there is evaluation of the unstructured coarse grids and heterogeneous perforated domains. The results for parabolic and thermoelasticity problems are given in Appendixes A and B .

5.1. Results for Elliptic Equation

We consider the elliptic equation in the perforated domain Ω with $k = 1$ and the following boundary conditions:

- *Case 1.* Homogeneous boundary conditions on perforations:

$$u = 1, \quad x \in \Gamma_g, \quad -k\nabla u \cdot n = \alpha u, \quad x \in \Gamma_p.$$

- *Case 2.* Non-homogeneous boundary conditions on perforations:

$$u = 0, \quad x \in \Gamma_g, \quad -k\nabla u \cdot n = \alpha(u - 1), \quad x \in \Gamma_p.$$

We consider three different $\alpha = 1, 25$, and 100.

Tables 1 and 2 show relative errors for elliptic problem with different perforation boundary coefficient $\alpha = 1, 25$, and 100. Here, M is the number of multiscale basis functions, and DOF_h and DOF_H are the numbers of degrees of freedom for fine-grid (reference) solution and multiscale solution. Here, $DOF_h = 3 \cdot N^h_{cell}$ for fine grid solution, where N^h_{cell} is the number of fine grid cells. For multiscale solution, $DOF_H = (M_g + 1) \cdot N_g + M_p \cdot N_p$, where $N_g = N^H_{cell}$ is the total number of coarse grid cells, and $N_p = N^H_{cell,p}$ is the number of coarse grid cells with perforations. For the problem with homogeneous boundary

conditions (Case 1), we use multiscale space without perforation basis functions ($M_p = 0$). Results for multiscale spaces with and without perforation boundary basis functions ($M_p = M$) are presented for Case 2 with non-homogeneous boundary conditions. For Case 1, we observe that the relative error in L^2 norm is reduced to 1% for $\alpha = 1, 25$, and 100, when we take the sufficient number of multiscale basis functions ($M_g = 12$ and $M_p = 0$). For Case 2 of the boundary conditions, the multiscale method gives a solution with a large error when perforation boundary multiscale basis functions is not taken ($M_p = 0$). However, we obtain good results after adding perforation boundary bases ($M_p = M$). For example, the relative L^2 error for $M = 12$ multiscale basis functions is 12% for $M_p = 0$ and reduced to 1.2% for $M_p = M$ ($\alpha = 25$). For the test problem with larger $\alpha = 100$, L^2 error from 21% to 0.67% is reduced. The graphical representation of the Tables 1 and 2 is given in Figure 8.

Table 1. Elliptic problem with $\alpha = 1, 25$, and 100. Case 1 (homogeneous boundary conditions). Relative L^2 and H^1 error in %. DOF_h = 85,230.

| M	DOF_H	$\alpha = 1$		$\alpha = 25$		$\alpha = 100$	
		e_{L^2}	e_{H^1}	e_{L^2}	e_{H^1}	e_{L^2}	e_{H^1}
		$M_g = M, M_p = 0$					
1	200	21.92	97.44	96.75	100.0	82.12	100.0
2	300	21.50	95.89	87.83	100.0	66.43	100.0
4	500	7.770	42.57	8.408	32.53	5.417	32.01
6	700	3.382	29.49	4.307	27.96	3.260	27.66
8	900	2.096	21.91	2.509	21.20	1.905	20.11
12	1300	1.201	14.33	1.417	13.33	1.053	13.08
16	1700	1.169	13.89	1.379	12.77	1.004	12.49
20	2100	1.127	13.10	1.349	12.03	0.972	11.81
24	2500	1.116	13.01	1.341	11.95	0.964	11.74
32	3300	1.098	12.80	1.329	11.74	0.957	11.53
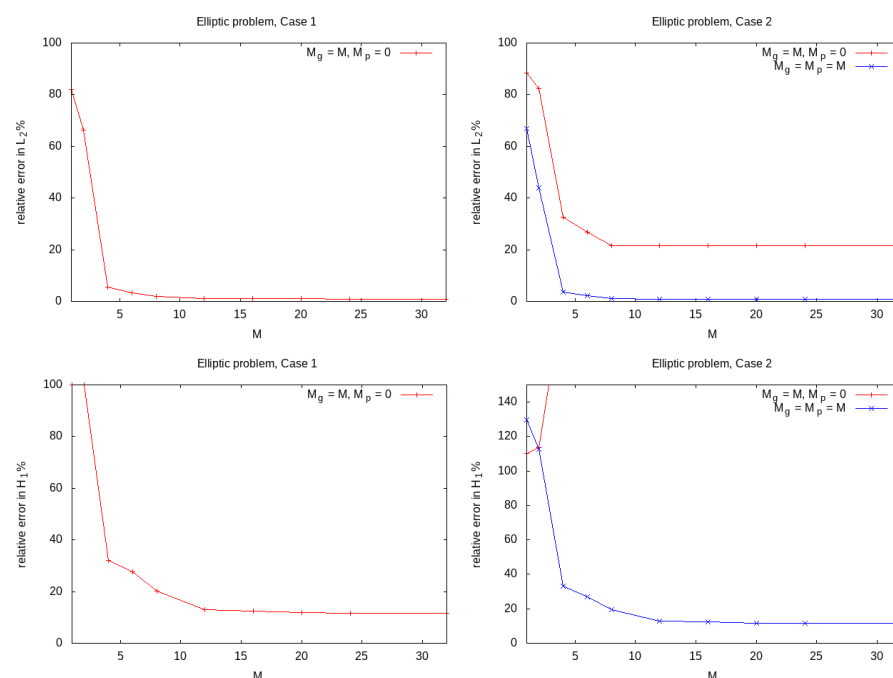
Figure 8. Elliptic problem with $\alpha = 100$. Case 1 (**left**) and Case 2 (**right**): Relative L_2(**top**) and H_1(**bottom**) error with a different number of multiscale basis functions.

Table 2. Elliptic problem with $\alpha = 1, 25$, and 100. Case 2 (non-homogeneous boundary conditions). Relative L^2 and H^1 error in %. DOF_h = 85,230.

M	DOF_H	$\alpha = 1$		$\alpha = 25$		$\alpha = 100$	
		e_{L^2}	e_{H^1}	e_{L^2}	e_{H^1}	e_{L^2}	e_{H^1}
		$M_g = M, M_p = 0$					
1	200	98.00	100.0	90.85	103.2	88.31	110.1
2	300	96.16	98.57	84.23	101.8	82.39	113.5
4	500	35.55	50.93	17.47	131.8	32.63	200.6
6	700	16.33	41.68	14.37	136.5	26.66	223.9
8	900	10.71	37.02	12.64	137.5	21.48	238.5
12	1300	6.896	33.31	12.29	136.9	21.52	237.5
16	1700	6.757	33.12	12.29	136.8	21.58	237.4
20	2100	6.580	32.80	12.29	136.7	21.63	237.1
24	2500	6.532	32.76	12.29	136.7	21.67	236.9
32	3300	6.457	32.68	12.29	136.7	21.68	236.8
		$M_g = M_p = M$					
1	251	96.63	97.45	82.96	123.0	66.74	129.7
2	402	93.85	95.23	67.28	116.0	43.93	112.6
4	704	27.84	39.03	6.909	32.68	3.523	33.20
6	1006	12.24	27.74	3.399	27.01	2.316	26.94
8	1308	7.909	20.65	1.747	20.01	1.201	19.30
12	1776	5.238	14.20	1.234	13.17	0.772	12.94
16	2244	5.108	13.80	1.197	12.64	0.735	12.37
20	2644	4.934	13.04	1.165	11.92	0.708	11.71
24	3044	4.887	12.97	1.155	11.86	0.699	11.66
32	3844	4.812	12.78	1.142	11.69	0.692	11.48

Figures 9 and 10 show the fine-grid and multiscale solutions for the elliptic problem with $\alpha = 100$ for Case 1 and Case 2, respectively. DOF_h = 85,230 is a reference (fine-grid) solution. For multiscale solution, we used 12 multiscale basis functions ($M = 12$) for both Cases. We have $DOF_H = 1300$ for multiscale solution without perforation boundary basis functions in Case 1 and Case 2 ($M_g = M$, $M_p = 0$), and $DOF_H = 1776$ for multiscale solution with perforation boundary basis functions in Case 2 ($M_g = M_p = M$). Figure test1-elliptic shows a reference (fine grid) solution on the left and a multiscale solution on the right for Case 1. For Case 2, there are three pictures in Figure 10: reference solution on the left, multiscale solution with $M_g = M$, $M_p = 0$ in the center, and multiscale solution with $M_g = M_p = M$ on the right. For Case 1, the perforation boundary multiscale basis functions are not needed because of set homogeneous boundary conditions on perforations ($M_p = 0$). For Case 2, the multiscale solution without perforation boundary bases ($M_p = 0$) gives large errors, but very good results are obtained for multiscale solver after adding perforation bases to handle non-homogeneous boundary conditions on perforations ($M_p = M$).
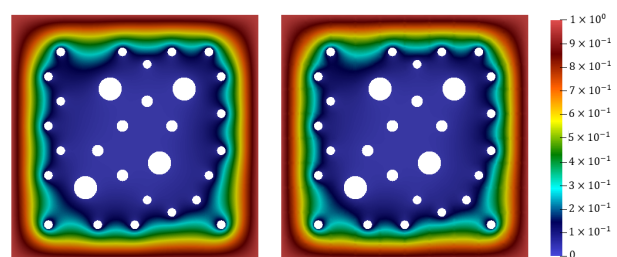

Figure 9. Elliptic problem with $\alpha = 100$. Case 1 (homogeneous boundary conditions). **Left**: Reference solution (DOF_h = 85,230). **Right**: Multiscale solution with 12 multiscale basis functions, $e_{L^2} = 1.053$ ($M_g = M = 12$, $M_p = 0$, $DOF_H = 1300$).
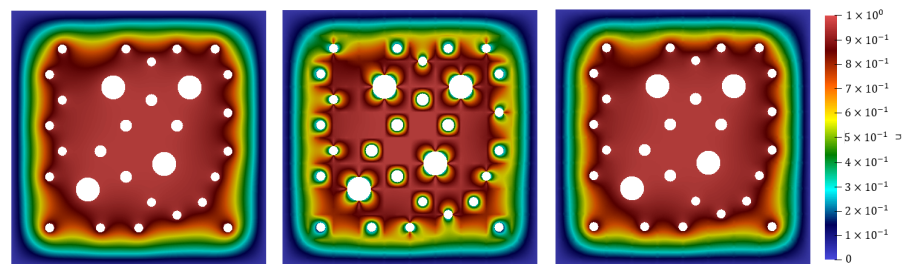
Figure 10. Elliptic problem with $\alpha = 100$. Case 2 (non-homogeneous boundary conditions). **Left:** Reference solution (DOF_h = 85,230). **Center**: Multiscale solution with 12 multiscale basis functions without perforation basis functions, $e_{L^2} = 21.52$ ($M_g = M = 12$, $M_p = 0$, $DOF_H = 1300$). **Right:** Multiscale solution with 12 multiscale basis functions with perforation basis functions, $e_{L^2} = 0.772$ ($M_g = M_p = M = 12$, $DOF_H = 1776$).

For Case 1 with homogeneous boundary conditions on perforations and Case 2 with non-homogeneous boundary conditions on perforations, based on results, it could be said that the presented multiscale method shows good results with small errors and demonstrates high accuracy for the both cases. Using non-homogeneous boundary conditions on perforations, the multiscale method using perforation boundary basis functions greatly improves results.

5.2. Results for Elasticity Equation

Let $\partial\Omega = \Gamma_t \cup \Gamma_b \cup \Gamma_l \cup \Gamma_r \cup \Gamma_p$, where $\Gamma_t, \Gamma_b, \Gamma_l, \Gamma_r$ be the top, bottom, left, and right boundaries.

We consider the elasticity equation with $\lambda = \mu = 1$ with the following boundary conditions:

$$u_x = 0, \quad \sigma_y = 0, \quad x \in \Gamma_l, \quad u_y = 0, \quad \sigma_x = 0, \quad x \in \Gamma_b,$$

and

- *Case 1.* Homogeneous boundary conditions on perforations:

$$\sigma \cdot n = 1, \quad x \in \Gamma_t \cup \Gamma_r, \quad \sigma \cdot n = 0, \quad x \in \Gamma_p.$$

- *Case 2.* Non-homogeneous boundary conditions on perforations:

$$\sigma \cdot n = 0, \quad x \in \Gamma_t \cup \Gamma_r, \quad \sigma \cdot n = -0.01, \quad x \in \Gamma_p.$$

Figures 11 and 12 show the results of the reference (fine-grid) and multiscale solutions for elasticity problem for Case 1 and Case 2. For illustration 24, multiscale basis functions ($M = 24$) are used. For fine grid solution, we have $DOF_h = 170,460$. $DOF_H = 4900$ is for the multiscale solution without perforation basis functions (Case 1 and Case 2) and $DOF_H = 5988$ for the multiscale solution with perforation boundary basis functions in Case 2. The displacements X-component is presented on the first row and Y-component on the second row. The first column shows the solutions on the fine grid. The second column shows the multiscale solution using outer boundary multiscale basis functions with $M_p = 0$ and $M_g = 24$. The third column for Case 2 shows a multiscale solution using outer and perforation boundary multiscale basis functions ($M_g = M_p = 24$). Here, $DOF_h = 6 \cdot N_{cell}^h$, $DOF_H = (2 \cdot M_g + 1) \cdot N_{cell}^H + 2 \cdot M_p \cdot N_{cell,p}^H$.
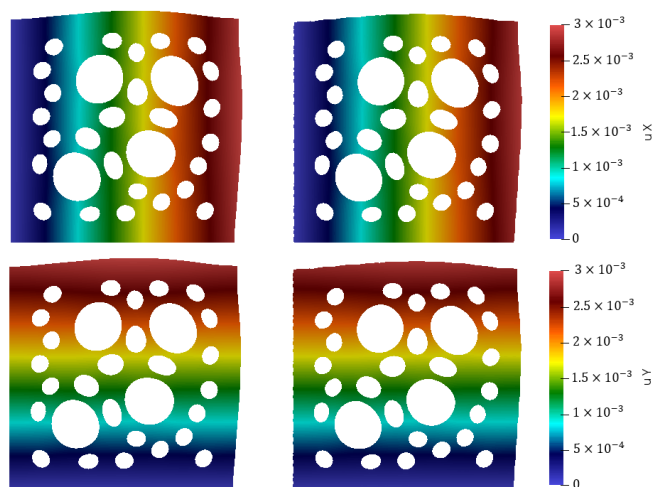
Figure 11. Elasticity problem. Case 1 (homogeneous boundary conditions). First row: displacement X-component. Second row: displacement Y-component. **Left:** Reference solution (DOF_h = 170,460). **Right:** Multiscale solution with 24 multiscale basis functions, e_{L^2} = 2.117 ($M_g = M = 24$, $M_p = 0$, $DOF_H = 4900$).
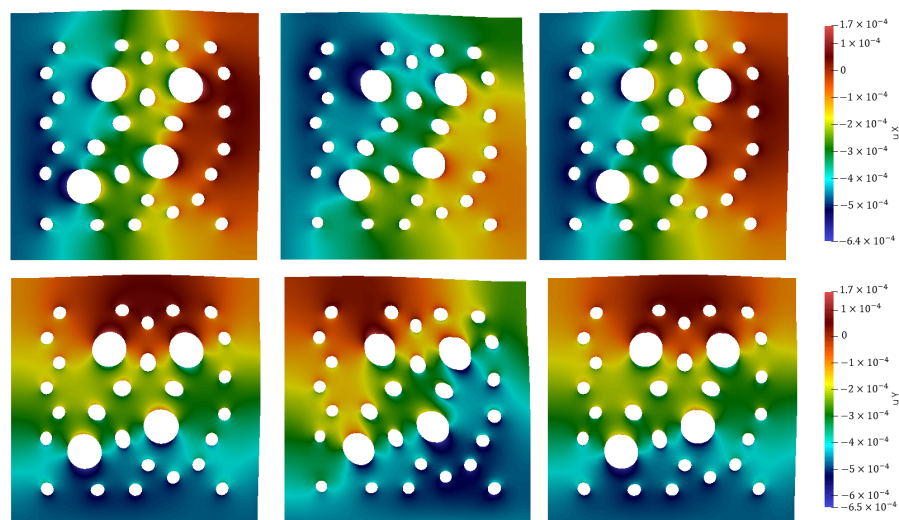
Figure 12. Elasticity problem. Case 2 (non-homogeneous boundary conditions). First row: displacement X-component. Second row: displacement Y-component. **Left:** Reference solution (DOF_h = 170,460). **Center:** Multiscale solution with 24 multiscale basis functions without perforation basis functions, e_{L^2} = 117.3 ($M_g = M = 24$, $M_p = 0$, $DOF_H^u = 4900$). **Right:** Multiscale solution with 24 multiscale basis functions with perforation basis functions, e_{L^2} = 2.324 ($M_g = M_p = M = 24$, $DOF_H^u = 5988$).

Tables 3 and 4 and Figure 13 present relative errors for elasticity problem for Case 1 and Case 2, respectively. Evidently the L^2 error reduce from 117% for $M_p = 0$ to 2.3% for $M_p = M$ in Case 2 with $M = 24$. For Case 1, we have 2% of L^2 error for $M_g = M = 24$ with $M_p = 0$. For both cases, we obtain good results with a sufficient number of multiscale basis functions.

Table 3. Elasticity problem. Case 1 (homogeneous boundary conditions). Relative L^2 and H^1 error in %. DOF_h = 170,460.

M	DOF_H	e_{L^2}	e_{H^1}
$M_g = M, M_p = 0$			
1	300	95.47	100.0
2	500	94.41	99.24
4	900	73.76	82.19
6	1300	14.50	32.53
8	1700	8.312	26.82
12	2500	6.031	22.41
16	3300	2.566	18.72
20	4100	2.354	18.08
24	4900	2.117	17.59
32	6500	1.893	17.49

Table 4. Elasticity problem. Case 2 (non-homogeneous boundary conditions). Relative L^2 and H^1 error in %. DOF_h = 170,460.

M	DOF_H	e_{L^2}	e_{H^1}	M	DOF_H	e_{L^2}	e_{H^1}
$M_g = M, M_p = 0$				$M_g = M, M_p = 0$			
1	300	113.2	84.90	1	402	98.24	70.33
2	500	111.9	83.33	2	704	92.46	65.32
4	900	119.7	72.36	4	1308	52.99	45.22
6	1300	118.0	64.02	6	1912	8.847	26.20
8	1700	117.5	60.98	8	2516	6.835	20.38
12	2500	117.6	59.82	12	3452	5.762	17.84
16	3300	117.4	59.50	16	4388	2.745	16.50
20	4100	117.4	59.37	20	5188	2.568	16.20
24	4900	117.3	59.29	24	5988	2.324	14.24
32	6500	117.2	58.35	32	7588	2.019	13.20

In Case 1 with homogeneous boundary conditions for elasticity on perforations, good results with outer basis functions are obtained. In Case 2 with non-homogeneous boundary conditions for elasticity on perforations, it is seen that, for displacement, we should use perforation boundary basis functions in order to approximate the non-homogeneous boundary condition.

5.3. Unstructured Coarse Grids

We consider a solution of the elliptic and elasticity problems using the presented multiscale method on quasi-structured and unstructured coarse grids. Figure 14 presents quasi-structured and unstructured coarse grids with an illustration of the local domains. Coarse grids contain 100 local domains. Problems with Case 2 boundary conditions are considered for numerical investigation.

Table 5 presents results for elliptic equation with $\alpha = 100$ for non-homogeneous boundary conditions (Case 2). The results for elasticity equation are presented in Table 6. Numerical results are shown for multiscale space with outer and boundary basis functions ($M_g = M_p = M$) on quasi-structured and unstructured coarse grids with 100 local domains. Using 32 multiscale basis functions ($M_p = M_g = 32$), similar results are obtained with less than 1% of L^2 error for structured, quasi-structured, and unstructured coarse grids with 100 local domains with $DOF_H = 3844$ (4.5% of $DOF_f = 85{,}230$). By comparing results with less number of multiscale basis functions ($M_p = M_g = 8$), it is observed that the error for structured coarse grid is smaller (1% and 19% for L^2 and H^1 errors) than for unstructured coarse grid (4.9% and 33% for L^2 and H^1 errors). Furthermore, the results show that the quasi-structured grid give a smaller errors than unstructured coarse grid (2% and 23% for L^2 and H^1 errors). For the elasticity problem with $M = 32$, we have 2% and 13% for L^2 and

H^1 errors for structured grid, 3% and 15% for L^2 and H^1 errors for quasi-structured grid, and 5% and 22% for L^2 and H^1 errors for unstructured grid.
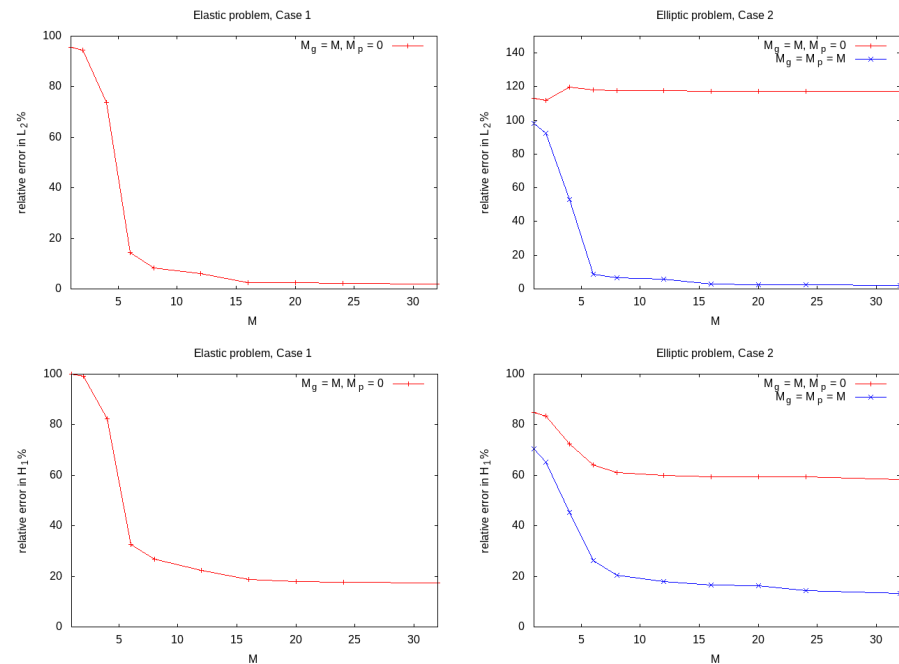
Figure 13. Elasticity problem. Case 1 (**left**) and Case 2 (**right**): Relative L_2(**top**) and H_1(**bottom**) error with a different number of multiscale basis functions.
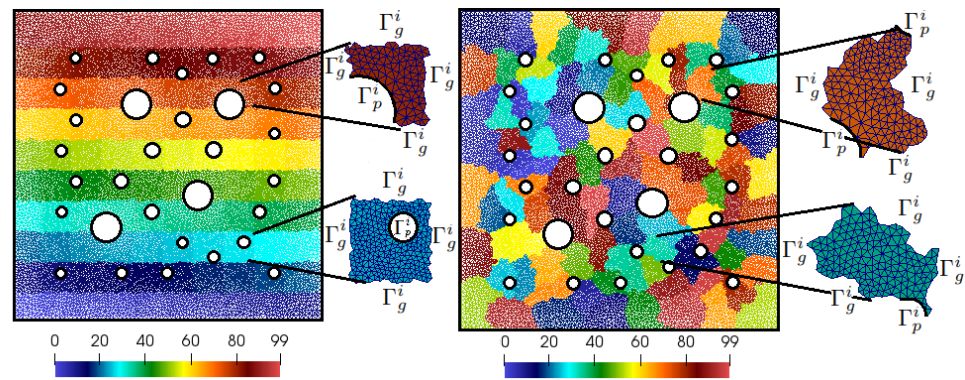
Figure 14. Coarse grids and local domains. (**Left**): quasi-structured grid. (**Right**): unstructured grid.

For elasticity problem with a smaller number of multiscale basis functions, there less errors for a structured grid than an unstructured grid. By comparison of the quasi-structured and unstructured grids, we see less errors for the quasi-structured coarse grid. Good results with less errors for any coarse grids can be obtained with a large number of multiscale basis functions. It should be noted that the main advantage of using unstructured coarse grids is the similar number of cells in each local domain (load balancing). Conforming triangulation of the domain with coarse edges is used in construction of the structured grid, which can be difficult for complex geometries with a large number of perforations. Though the conforming construction is not needed in the quasi-structured grid. Numerical results show that the presented multiscale method works very well with any coarse grid construction concepts.

Table 5. Elliptic problem. Case 2 (non-homogeneous boundary conditions). Unstructured coarse grids. Relative L^2 and H^1 error in %. DOF_h = 85,230.

M	DOF_H	Quasi-Structured		Unstructured	
		e_{L^2}	e_{H^1}	e_{L^2}	e_{H^1}
1	251	58.12	101.1	56.66	98.80
2	402	35.39	87.82	45.87	104.1
4	704	6.539	41.82	16.53	60.94
6	1006	3.523	33.69	9.504	43.29
8	1308	2.034	23.72	4.909	33.93
12	1776	1.369	19.11	2.187	25.77
16	2244	1.052	17.04	1.390	22.29
20	2644	0.896	15.76	0.994	19.81
24	3044	0.783	15.06	0.734	17.48
32	3844	0.683	14.33	0.552	15.83

Table 6. Elasticity problem. Case 2 (non-homogeneous boundary conditions). Unstructured coarse grids. Relative L^2 and H^1 error in %. DOF_h = 170,460.

M	DOF_H	Quasi-Structured		Unstructured	
		e_{L^2}	e_{H^1}	e_{L^2}	e_{H^1}
1	402	89.14	63.53	97.97	83.36
2	704	82.55	59.52	94.60	77.88
4	1308	62.82	49.96	76.75	66.07
6	1912	44.10	41.86	50.62	53.07
8	2516	20.71	30.19	29.94	43.22
12	3452	13.68	24.60	15.75	32.33
16	4388	8.648	20.83	10.57	27.54
20	5188	6.682	18.96	8.107	25.11
24	5988	5.309	17.49	6.705	23.75
32	7588	3.629	15.64	5.407	22.26

5.4. Heterogeneous Coefficients

Finally, we consider the efficiency of the presented method for the solution of the elliptic and elasticity problems with heterogeneous coefficients ($k = k(x)$ and $E = E(x)$). The heterogeneous elasticity parameter and heterogeneous diffusion coefficient are presented in Figure 15. The parameters λ and μ are given as follows:

$$\mu(x) = \frac{E(x)}{2(1+\nu)}, \quad \lambda(x) = \frac{E(x)\nu}{(1+\nu)(1-2\nu)},$$

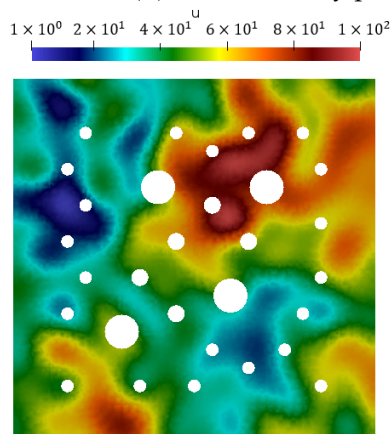where $E = E(x)$ is the elasticity parameter, and $\nu = 0.3$ is the constant Poisson's ratio.

Figure 15. Heterogeneous coefficient.

Table 7 presents the relative L_2 and H_1 errors for elliptic (left) and elasticity (right) problems with heterogeneous coefficients. Case 2 with non-homogeneous boundary conditions for perforation is considered ($M_g = M_p = M$). For elliptic problem, the results are presented with $\alpha = 100$. Numerical results for elliptic and elasticity problems show that the presented multiscale method works well with heterogeneous coefficients.

Table 7. Elliptic and elasticity problem with heterogeneous coefficients. Case 2 (non-homogeneous boundary conditions). Relative L^2 and H^1 error in %.

M	Elliptic Problem			Elasticity Problem		
	DOF_H	e_{L^2}	e_{H^1}	DOF_H	e_{L^2}	e_{H^1}
1	251	57.72	96.62	402	108.1	76.69
2	402	52.28	91.43	704	105.4	69.97
4	704	16.86	40.61	1308	44.45	44.88
6	1006	11.68	29.68	1912	9.455	29.43
8	1308	4.498	23.30	2516	6.824	23.97
12	1776	2.979	16.56	3452	4.753	21.43
16	2244	3.170	14.98	4388	3.511	20.25
20	2644	3.078	14.35	5188	3.327	19.97
24	3044	3.258	13.75	5988	3.235	19.90
32	3844	3.199	13.65	7588	3.024	17.95

6. Conclusions

This paper presents the multiscale method for solution problems in the perforated domain with non-homogeneous boundary conditions on perforations. For approximation on the fine grid that resolved perforations on the grid level, we apply the Discontinuous Galerkin finite element method and use the solution as a reference solution. To reduce the size of the fine grid system, we present a Discontinuous Galerkin Generalized Multiscale Finite Element Method (DG-GMsFEM) with the construction of two types of multiscale basis functions for subdomain boundary and perforation boundary, separately. Presented perforation boundary basis functions are used to approximate non-homogeneous boundary conditions on perforations. Numerical investigation of the presented method was performed for four model problems: (1) elliptic, (2) parabolic, (3) elasticity, and (4) thermoelasticity problems in the perforated domain. The results for two cases with homogeneous and non-homogeneous boundary conditions are given. For the case with homogeneous boundary conditions on perforations, the given results are obtained using only subdomain boundary basis functions. However, for a non-homogeneous boundary condition, both subdomain and perforation boundary basis functions should be used. Numerical results are presented for different concepts of the coarse grid construction (structured, quasi-structured, and unstructured coarse grids). Numerical results show that the proposed method can provide good results and give a significant reduction of the system size with appropriate choosing construction of the multiscale basis functions for problems with homogeneous and non-homogeneous perforation boundary conditions. In future works, we plan to consider oversampling techniques for multiscale basis function construction, construct a multiscale solver for three-dimensional problems, and consider construction of the accurate multiscale techniques for nonlinear problems in heterogeneous perforated media.

Author Contributions: Conceptualization, M.V. and E.T.C.; methodology, M.V., E.C. and V.A.; software, V.A. and U.K.; validation, V.A., M.V. and U.K.; formal analysis, M.V.; investigation, V.A.; resources, V.A., U.K.; data curation, M.V., V.A.; writing—original draft preparation, V.A.; writing—review and editing, M.V., U.K., E.T.C. and V.A.; visualization, V.A.; supervision, M.V., E.T.C.; project administration, M.V.; funding acquisition, V.A. All authors have read and agreed to the published version of the manuscript.

Institutional Review Board Statement: Not applicable.

Informed Consent Statement: Not applicable.

Data Availability Statement: Not applicable.

Conflicts of Interest: The authors declare no conflict of interest.

Appendix A. Parabolic Problem

We consider the parabolic problem in perforated domain Ω:

$$\frac{\partial u}{\partial t} - \nabla \cdot (k \nabla u) = 0, \quad x \in \Omega \tag{A1}$$

with the following boundary conditions

$$u = g_g, \quad x \in \Gamma_g, \quad -k \nabla u \cdot n = \alpha(u - g_p), \quad x \in \Gamma_p,$$

and initial condition $T = T_0$ in Ω for $t = 0$.

For approximation by time, we use an implicit approximation with a time step τ. We have the following fine grid approximation on $\mathcal{T}^h$ using the IPDG method: find $u_h \in V_h$ such that

$$\frac{1}{\tau} m(u_h - \breve{u}_h, v) + a(u_h, v) = l(v), \quad \forall v \in V_h,$$

where

$$a(u, v) = \sum_{K \in \mathcal{T}^h} \int_K (k \nabla u, \nabla v) \, dx + \sum_{E \in \mathcal{E}_{b,p}^h} \int_E \alpha \, u \, v \, ds$$

$$- \sum_{E \in \mathcal{E}_o^h \cup \mathcal{E}_{b,g}^h} \int_E \left(\{k \nabla u \cdot n\} \cdot [v] + \{k \nabla v \cdot n\} \cdot [u] - \frac{\gamma_f}{h} \{k\} [u] \cdot [v] \right) ds,$$

$$l(v) = \sum_{E \in \mathcal{E}_{b,p}^h} \int_E \alpha \, g_p \, v \, ds + \sum_{E \in \mathcal{E}_{b,g}^h} \int_E \left(\frac{\gamma_f}{h} k \, v - k \nabla v \cdot n \right) g_g \, dx, \quad m(u, v) = \sum_{K \in \mathcal{T}^h} \int_K u \, v \, ds,$$

and $\breve{u}_h$ is the solution from the previous time step.

The matrix form is following

$$\frac{1}{\tau} M_h (U_h - \breve{U}_h) + A_h (U_h) = F_h,$$

for $u_h = \sum_i U_i \varphi_i$ and with

$$M_h = [m_{i,j} := m(\varphi_i, \varphi_j)], \quad A_h = [a_{i,j} := a(\varphi_i, \varphi_j)], \quad F_h = [f_j := l(\varphi_j)].$$

In the multiscale method, we construct a multiscale space similar to the Laplace problem and generate a projection matrix

$$R = \left[\varphi_{g,1}^1, \ldots, \varphi_{g,M_g}^{N_g}, \varphi_{p,1}^2, \ldots, \varphi_{p,M_p}^{N_p}, \varphi_1, \ldots, \varphi_{N_{cell}^H} \right]^{Tr}.$$

Finally, we obtain the following coarse grid system for a parabolic problem

$$\frac{1}{\tau} M_H (U_H - \breve{U}_H) + A_H (U_H) = F_H,$$

where

$$M_H = R M_h R^{Tr}, \quad A_H = R A_h R^{Tr}, \quad F_H = R F_h,$$

and calculation of the coarse-scale solution, we reconstruct the fine-scale solution $U_{ms} = R^{Tr} U_H$.

Numerical results. We consider the parabolic problem with $k = 1$. We set the following boundary conditions:

- *Case 1.* Homogeneous boundary conditions on perforations:

$$u = 1, \quad x \in \Gamma_g, \quad -k\nabla u \cdot n = \alpha u, \quad x \in \Gamma_p,$$

　and perform simulation for $t_{max} = 0.02$.

- *Case 2.* Non-homogeneous boundary conditions on perforations:

$$u = 0, \quad x \in \Gamma_g, \quad -k\nabla u \cdot n = \alpha(u - 1), \quad x \in \Gamma_p.$$

　and perform simulation for $t_{max} = 0.01$.

We consider three different $\alpha = 1, 25$, and 100. We set zero initial condition and perform a simulation with 40 time steps.
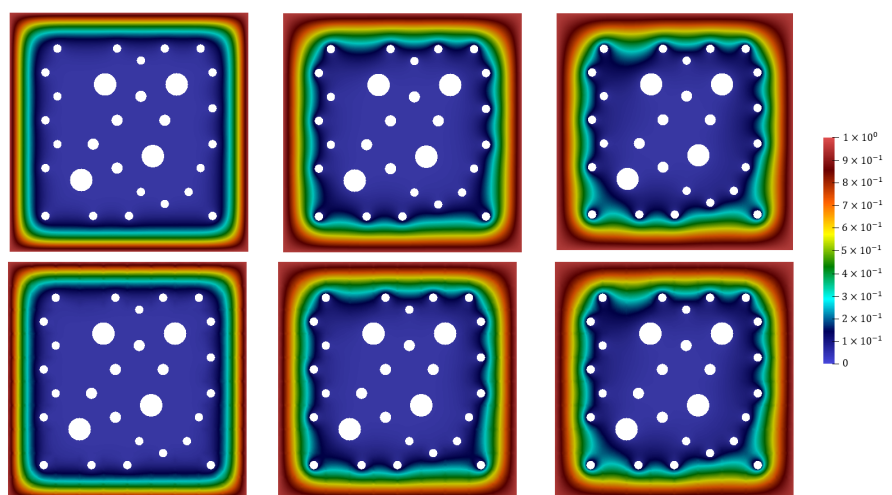

Figure A1. Parabolic problem with $\alpha = 100$ for different time layers t_m with $m = 5, 15$, and 40 (from **left** to **right**). Case 1 (homogeneous boundary conditions). **Top**: Reference solution ($DOF_h = 85{,}230$). **Bottom**: Multiscale solution with 12 multiscale basis functions, $e_{L^2} = 2.22$ for t_1, $e_{L^2} = 1.605$ for t_{10}, $e_{L^2} = 1.058$ for t_{40} ($M_g = M = 12$, $M_p = 0$, $DOF_H = 1300$).

Table A1. Parabolic problem with $\alpha = 1, 25$, and 100. Case 1 (homogeneous boundary conditions). Relative L^2 and H^1 error in %. $DOF_h = 85{,}230$.

| M	DOF_H	$\alpha = 1$		$\alpha = 25$		$\alpha = 100$	
		e_{L^2}	e_{H^1}	e_{L^2}	e_{H^1}	e_{L^2}	e_{H^1}
		$M_g = M, M_p = 0$					
1	200	86.14	99.75	101.6	134.7	83.13	157.8
2	300	85.57	99.22	92.55	124.4	67.41	130.3
4	500	18.58	34.51	9.460	32.42	5.393	31.97
6	700	8.323	28.86	5.001	27.98	3.436	27.71
8	900	4.445	20.53	2.774	20.93	1.959	20.08
12	1300	2.870	14.32	1.734	13.33	1.164	13.10
16	1700	2.784	13.96	1.675	12.79	1.109	12.52
20	2100	2.693	13.28	1.635	12.06	1.076	11.84
24	2500	2.666	13.23	1.622	11.99	1.066	11.76
32	3300	2.625	13.09	1.604	11.79	1.058	11.56
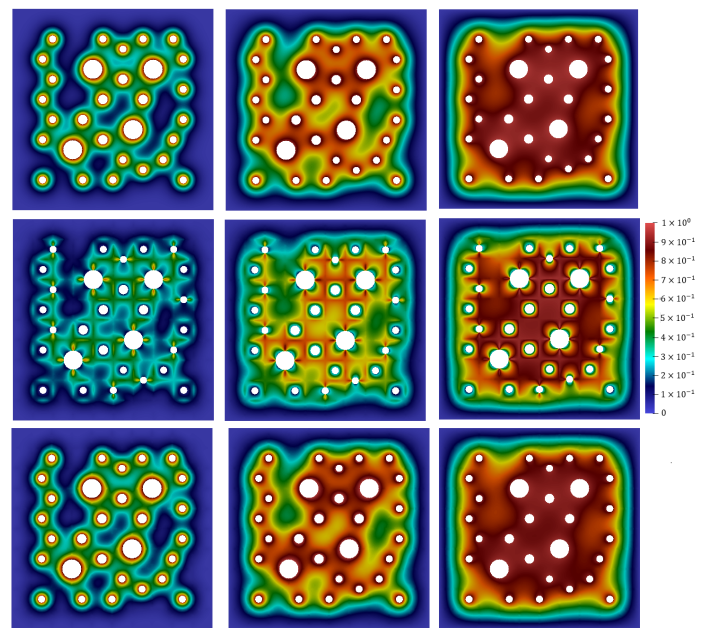
Figure A2. Parabolic problem with $\alpha = 100$ for different time layers t_m with $m = 5, 15$, and 40 (from **left** to **right**). Case 2 (non-homogeneous boundary conditions). **Top**: Reference solution ($DOF_h = 85{,}230$). **Center**: Multiscale solution with 12 multiscale basis functions without perforation basis functions, $e_{L^2} = 46.53$ for t_5, $e_{L^2} = 35.14$ for t_{15}, and $e_{L^2} = 22.84$ for t_{40} ($M_g = 12$, $M_p = 0$, $DOF_H = 1300$). **Bottom**: Multiscale solution with 12 multiscale basis functions with perforation basis functions, $e_{L^2} = 2.506$ for t_5, $e_{L^2} = 1.621$ for t_{15}, and $e_{L^2} = 0.742$ for t_{40} ($M_g = M_p = M = 12$, $DOF_H = 1776$).
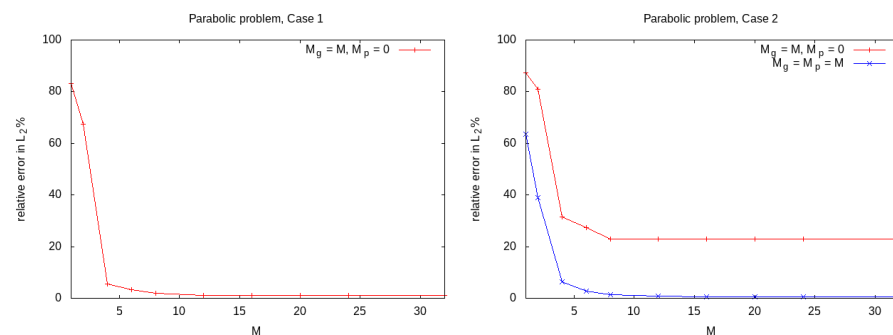
Figure A3. Parabolic problem with $\alpha = 100$ at the final time. Case 1 (**left**) and Case 2 (**right**): Relative L_2 error with a different number of multiscale basis functions.

The reference and multiscale solutions at the different times (t_m with $m = 5, 15$, and 40) are presented in Figure A1 for Case 1 and in Figure A2 for Case 2. The multiscale solution is obtained using 12 multiscale basis functions ($M = 12$). In the first row, there is a fine-scale solution with $DOF_h = 85{,}230$. In the second row, there is a multiscale solution with $DOF_H = 1300$ for $M_p = 0$. In the third row, we give a multiscale solution with $DOF_H = 1776$ for $M_p = M$ in Case 2. We observe a bad multiscale approximation near the perforation boundary for Case 2 with $e_{L^2} = 22\%$ at final time, if a perforation boundary basis functions is not used to handle non-homogeneous boundary conditions. For $M_p = M$ in Case 2, we observe a good multiscale solution with $e_{L62} = 0.7\%$ at final time.

Table A2. Parabolic problem with $\alpha = 1, 25$, and 100. Case 2 (non-homogeneous boundary conditions). Relative L^2 and H^1 error in %. $DOF_h = 85,230$.

M	DOF_H	$\alpha = 1$		$\alpha = 25$		$\alpha = 100$	
		e_{L^2}	e_{H^1}	e_{L^2}	e_{H^1}	e_{L^2}	e_{H^1}
		$M_g = M, M_p = 0$					
1	200	91.97	100.0	88.25	106.2	87.32	113.5
2	300	84.84	98.29	79.71	107.8	80.87	119.0
4	500	13.88	79.31	17.52	146.2	31.49	209.5
6	700	9.709	74.94	15.97	148.1	27.40	228.8
8	900	8.124	72.15	14.66	147.7	22.90	240.5
12	1300	7.552	71.39	14.83	147.6	22.84	238.9
16	1700	7.330	68.91	14.40	146.1	22.90	238.7
20	2100	7.289	68.60	14.41	145.9	22.96	238.4
24	2500	7.280	68.49	14.42	145.8	22.99	238.2
32	3300	7.264	68.39	14.42	145.8	23.01	238.1
		$M_g = M_p = M$					
1	251	85.93	79.07	77.39	103.4	63.56	116.3
2	402	75.40	75.78	57.40	99.07	38.96	101.3
4	704	7.938	38.96	5.154	35.27	6.326	36.65
6	1006	4.084	29.37	2.857	27.33	2.897	26.93
8	1308	2.339	21.96	1.566	20.95	1.394	19.50
12	1776	1.289	14.29	0.819	13.35	0.742	12.92
16	2244	1.192	13.19	0.735	12.54	0.654	12.24
20	2644	1.129	12.19	0.701	11.78	0.619	11.59
24	3044	1.117	11.90	0.691	11.61	0.603	11.49
32	3844	1.093	11.59	0.677	11.36	0.588	11.28

Table A3. Parabolic problem. Case 2 (non-homogeneous boundary conditions). Unstructured coarse grids. Relative L^2 and H^1 error in %. $DOF_h = 85,230$.

M	DOF_H	Quasi-Structured		Unstructured	
		e_{L^2}	e_{H^1}	e_{L^2}	e_{H^1}
1	251	54.82	96.18	53.32	93.48
2	402	30.56	79.76	41.23	94.00
4	704	8.184	45.51	11.60	56.13
6	1006	4.889	34.72	6.561	41.29
8	1308	3.434	25.08	4.976	35.25
12	1776	3.944	23.14	3.725	27.85
16	2244	1.526	17.72	2.761	23.90
20	2644	1.209	16.25	2.063	21.00
24	3044	0.999	15.26	1.775	18.64
32	3844	0.803	14.43	1.429	16.74

The relative errors for parabolic problem (Case 1) between reference solution and multiscale solution for $\alpha = 1, 25$, and 100 are shown in Table A1 and in Figure A3 (left picture). We have a good multiscale solution with nearly 1–2% of L^2 error when we take 12 outer boundary multiscale basis functions. Table A2 and Figure A3 (right picture) present relative errors for Case 2. Similar to the previous results for the elliptic equation, we see large errors for $M_p = 0$ and can obtain a good multiscale solution when we take the sufficient number of multiscale basis functions with outer and perforation boundary multiscale basis functions. For example, if 12 multiscale basis functions ($M = 12$) are taken, we have 7–22% of L^2 errors for $M_p = 0$ and reduce errors to 1% when we add perforation boundary basis functions for $\alpha = 1, 25$, and 100.

Table A3 shows results for non-homogeneous boundary conditions (Case 2) on quasi-structured and unstructured coarse grids with 100 local domains. We present results for $\alpha = 100$. Using 32 multiscale basis functions ($M_p = M_g = 32$), we obtain similar results with less than 1% of L^2 error for structured, quasi-structured, and unstructured coarse grids with 100 local domains with $DOF_H = 3844$ (4.5% of $DOF_f = 85,230$).

Appendix B. Thermoelasticity Problem

We consider the thermoelasticity problem in Ω that is described by a system of equations for temperature and displacement:

$$
\begin{aligned}
\nabla \cdot \sigma(u) - \beta \nabla (T - T_*) &= 0, \quad x \in \Omega, \\
c\frac{\partial T}{\partial t} + \beta \frac{\partial \nabla \cdot u}{\partial t} - \nabla \cdot (k\nabla T) &= 0, \quad x \in \Omega,
\end{aligned} \tag{A2}
$$

We consider Equation (A2) with the following boundary conditions:

$$
u = g_g^u, \quad T = g_g^T, \quad x \in \Gamma_g, \quad \sigma \cdot n = g_p^u, \quad -k\nabla T \cdot n = \alpha(T - g_p^T), \quad x \in \Gamma_p,
$$

and initial condition $T = T_0$, $u = 0$ in Ω for $t = 0$.

For the IPDG method on the fine grid $\mathcal{T}^h$, we have the following variational formulation: find $(u_h, T_h) \in W_h \times Q_h$ such that

$$
\begin{aligned}
a^u(u_h, v) + b(T_h, v) &= l^u(v), \quad \forall v \in W_h \\
\frac{1}{\tau}m(T_h - \check{T}_h, q) + \frac{1}{\tau}d(u_h - \check{u}_h, q) + a^T(T_h, q) &= l^T(q), \quad \forall q \in Q_h
\end{aligned}
$$

where

$$
\begin{aligned}
Q_h &= \{T \in L^2(\Omega) : T|_K \in \mathbb{P}_1(K), \forall K \in \mathcal{T}^h\} \\
W_h &= \{v \in [L^2(\Omega)]^2 : v|_K \in [\mathbb{P}_1(K)]^2, \forall K \in \mathcal{T}^h\},
\end{aligned}
$$

with

$$
\begin{aligned}
a^T(T, q) &= \sum_{K \in \mathcal{T}^h} \int_K (k\nabla T, \nabla q)\, dx + \sum_{E \in \mathcal{E}_{b,p}^h} \int_E \alpha\, T\, q\, ds \\
&\quad - \sum_{E \in \mathcal{E}_o^h \cup \mathcal{E}_{b,g}^h} \int_E \left(\{k\nabla T \cdot n\} \cdot [q] + \{k\nabla q \cdot n\} \cdot [T] - \frac{\gamma_f}{h}\{k\}[T] \cdot [q] \right) ds,
\end{aligned}
$$

$$
l(q) = \sum_{E \in \mathcal{E}_{b,p}^h} \int_E \alpha\, g_p^T\, q\, ds + \sum_{E \in \mathcal{E}_{b,g}^h} \int_E \left(\frac{\gamma_f}{h} k\, q - k\nabla q \cdot n \right) g_g^T\, dx,
$$

$$
m(T, q) = \sum_{K \in \mathcal{T}^h} \int_K c\, T\, q\, dx,
$$

$$
\begin{aligned}
a^u(u, v) &= \sum_{K \in \mathcal{T}^h} \int_K (\sigma(u), \varepsilon(v))\, dx \\
&\quad - \sum_{E \in \mathcal{E}_o^h \cup \mathcal{E}_{b,g}^h} \int_E \left(\{\tau(u)\}[v] + \{\tau(v)\}[u] - \frac{\gamma_f}{h}\{\lambda + 2\mu\}[u][v] \right) ds,
\end{aligned}
$$

$$
l^u(v) = \sum_{E \in \mathcal{E}_{b,p}^h} \int_E g_p^u \cdot v\, ds + \sum_{E \in \mathcal{E}_{b,g}^h} \int_E \left(\frac{\gamma_f}{h}(\lambda + 2\mu)v - \tau(v) \right) \cdot g_g^u\, ds,
$$

$$
b(T, v) = \sum_{K \in \mathcal{T}^h} \int_K \beta\, \nabla T \cdot v\, dx, \quad d(u, q) = \sum_{K \in \mathcal{T}^h} \int_K \beta\, \nabla \cdot u\, q\, dx.
$$

The matrix form is the following:

$$
\begin{aligned}
A_h^u(U_h) + B_h(T_h) &= F_h^u \\
\frac{1}{\tau}M_h(T_h - \check{T}_h) + \frac{1}{\tau}D_h(U_h - \check{U}_h) + A_h^T(T_h) &= F_h^T,
\end{aligned}
$$

for

$$
u_h = \sum_i U_i \psi_i; \quad T_h = \sum_i T_i \varphi_i,
$$

with

$$M_h = [m_{i,j} := m(\varphi_i, \varphi_j)], \quad A_h^T = [a_{i,j}^T := a^T(\varphi_i, \varphi_j)], \quad A_h^u = [a_{i,j}^u := a^u(\psi_i, \psi_j)],$$

$$B_h = [b_{i,j} := b(\psi_i, \varphi_j)], \quad D_h = [d_{i,j} := d(\varphi_i, \psi_j)],$$

$$F_h^u = [f_j^u := l^u(\psi_j)], \quad F_h^T = [f_j^T := l^T(\varphi_j)].$$

For the construction of the multiscale method for the thermoelasticity problem, we construct multiscale spaces for displacement and temperature, separately. Then, we generate projection matrices using multiscale basis functions

$$R_u = \left[\psi_{g,1}^1, \ldots, \psi_{g,M_g^u}^{N_g}, \psi_{p,1}^2, \ldots, \psi_{p,M_p^u}^{N_p}, \phi_1, \ldots, \phi_{N_{cell}^H} \right]^{Tr},$$

$$R_T = \left[\varphi_{g,1}^1, \ldots, \varphi_{g,M_g^T}^{N_g}, \varphi_{p,1}^2, \ldots, \varphi_{p,M_p^T}^{N_p}, \varphi_1, \ldots, \varphi_{N_{cell}^H} \right]^{Tr}.$$

Finally, we construct the following coarse grid system for the thermoelasticity problem

$$A_H^u(U_H) + B_H(T_H) = F_H^u$$

$$\frac{1}{\tau} M_H(T_H - \check{T}_H) + \frac{1}{\tau} D_H(U_H - \check{U}_H) + A_H^T(T_H) = F_H^T,$$

where

$$M_H = R_T M_h R_T^{Tr}, \quad A_H^T = R_T A_h^T R_T^{Tr}, \quad A_H^u = R_u A_h^u R_u^{Tr},$$

$$B_H = R_u B_h R_T^{Tr}, \quad D_H = R_T D_h R_u^{Tr}, \quad F_H^u = R_u F_h^u, F_H^T = R_T F_h^T.$$

After calculation of the coarse-scale solution U_h, T_H, we reconstruct a fine-scale solution, $U_{ms} = R_u^{Tr} U_H$ and $T_{ms} = R_T^{Tr} T_H$.

Numerical results. We consider the thermoelasticity problem with the following boundary conditions:

$$u_x = 0, \quad \sigma_y = 0, \quad x \in \Gamma_l \cup \Gamma_r, \quad u_y = 0, \quad \sigma_x = 0, \quad x \in \Gamma_b \cup \Gamma_t,$$

$$-k \frac{\partial T}{\partial n} = 0, \quad x \in \Gamma_l \cup \Gamma_t \cup \Gamma_r \cup \Gamma_b,$$

and on perforations, we set

- *Case 1.* Non-homogeneous boundary condition for elasticity and homogeneous boundary condition for temperature on perforations:

$$\sigma \cdot n = -0.01, \quad -k \frac{\partial T}{\partial n} = \alpha T, \quad x \in \Gamma_p,$$

and perform simulation for $t_{max} = 0.15$.

- *Case 2.* Homogeneous boundary condition for elasticity and non-homogeneous boundary condition for temperature on perforations:

$$\sigma \cdot n = 0, \quad -k \frac{\partial T}{\partial n} = \alpha(T - 1), \quad x \in \Gamma_p,$$

and perform simulation for $t_{max} = 0.02$.

We set $\lambda = \mu = k = c = 1$, $T_* = 0$, $\beta = 0.0001$, and $\alpha = 25$. We set zero initial conditions for displacement and temperature and perform simulations with 40 time steps.
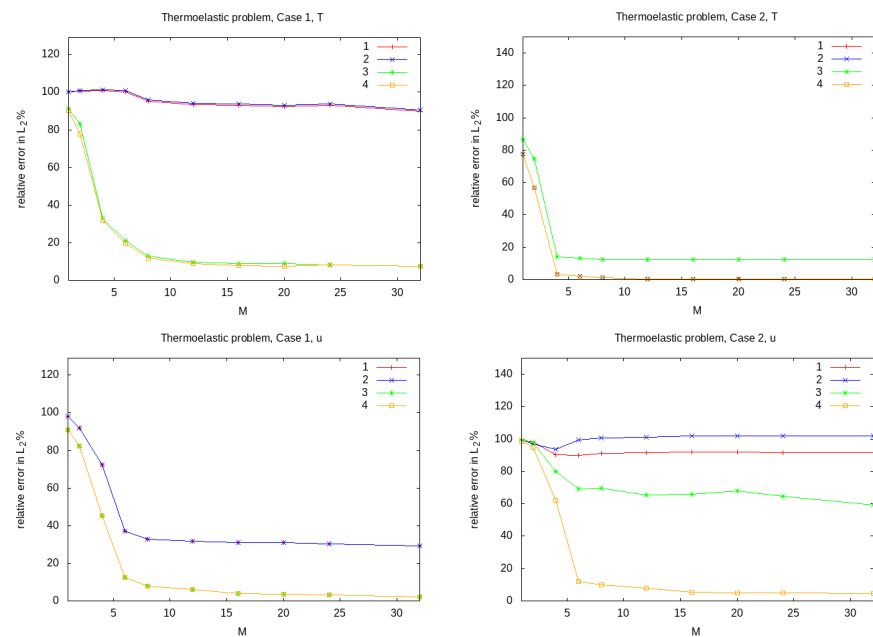
Figure A4. Thermoelasticity problem. Temperature (**top**) and Displacement (**bottom**). Case 1 and Case 2: Relative L_2 error with a different number of multiscale basis functions. (1) $M_g^u = M^u$, $M_p^u = 0$ and $M_g^T = M^T$, $M_p^T = 0$; (2) $M_g^u = M^u$, $M_p^u = 0$, and $M_g^T = M_p^T = M^T$; (3) $M_g^u = M_p^u = M^u$ and $M_g^T = M^T$, $M_p^T = 0$; (4) $M_g^u = M_p^u = M^u$ and $M_g^T = M_p^T = M^T$.

Table A4 and Figure A4 show relative errors for the thermoelasticity problem between a fine-grid and multiscale solution with different multiscale basis functions at the final time. In presented results, we tested different approaches for choosing M_g^u, M_p^u and M_g^T, M_p^T for the coupled process. Here, M^v are the number of multiscale basis functions for displacement ($v = u$) and temperature ($v = T$), DOF_h^v and DOF_H^v are the numbers of degrees of freedom for reference (fine-grid) and multiscale solution, and $e(v)_{L^2}$ and $e(v)_{H^1}$ are the L^2 and H^1 relative errors for $v = u, T$. Here, $DOF_h = DOF_h^u + DOF_h^T$ with $DOF_h^u = 6 \cdot N_{cell}^h$ and $DOF_h^T = 3 \cdot N_{cell}^h$ for fine grid solution. For multiscale solution, we have $DOF_H = DOF_H^u + DOF_H^T$ with $DOF_H^u = (2 \cdot M_g^u + 1) \cdot N_{cell}^H + 2 \cdot M_p^u \cdot N_{cell,p}^H$ and $DOF_H^T = (M_g^T + 1) \cdot N_{cell}^H + M_p^T \cdot N_{cell,p}^H$.

The results for quasi-structured and unstructured coarse grids with 100 local domains are presented in Table A5. Numerical results are shown for multiscale space with outer and boundary basis functions ($M_g = M_p = M$) for Case 2. We obtain similar results with 4% and 0.3% for displacement and temperature L^2 errors for all grids for $M = 32$.

Figures A5 and A6 show the results of the fine-grid and multiscale solvers for the thermoelasticity problem at the final time on structured coarse grid. The temperature distribution is presented on the left figure, the displacement X and Y components are shown in the center and right figures. In presented results, we used 24 multiscale basis functions for displacement and temperature ($M^u = M^T = 24$, $M_g^u = M_p^u = M^u$, and $M_g^T = M_p^T = M^T$). Reference solution with $DOF_h^u = 170,460$ for displacement, $DOF_h^T = 85,230$ for temperature is shown in the first row. Solution on a coarse grid using outer and perforation boundary multiscale basis functions with $DOF_H^u = 5988$ for displacement and $DOF_H^T = 3044$ for temperature is shown in the second row.

Table A4. Thermoelasticity problem. Case 1 and Case 2. $M = M^u = M^T$. Relative L^2 and H^1 error in %. $DOF_h = 170{,}460$.

M	DOF_H^u	DOF_H^T	Case 1				Case 2			
			$e(u)_{L^2}$	$e(u)_{H^1}$	$e(T)_{L^2}$	$e(T)_{H^1}$	$e(u)_{L^2}$	$e(u)_{H^1}$	$e(T)_{L^2}$	$e(T)_{H^1}$
$M_g^u = M^u,\ M_p^u = 0$ and $M_g^T = M^T,\ M_p^T = 0$										
1	300	200	98.00	99.98	100.0	100.0	99.32	98.98	86.48	105.9
2	500	300	92.01	98.38	100.6	100.4	98.04	97.07	74.55	106.3
4	900	500	72.44	93.63	100.9	98.37	90.47	73.54	14.16	142.4
6	1300	700	36.91	87.77	100.3	93.44	90.01	55.30	13.32	143.3
8	1700	900	32.73	85.34	95.06	87.08	91.23	50.41	12.36	143.4
12	2500	1300	31.88	84.32	93.31	85.43	91.41	48.40	12.25	142.2
16	3300	1700	31.03	83.99	93.04	85.05	91.85	47.36	12.26	142.1
20	4100	2100	30.86	83.82	92.43	84.44	91.79	47.07	12.28	142.0
24	4900	2500	30.37	84.07	92.89	84.64	91.69	47.56	12.30	141.9
32	6500	3300	29.31	82.66	89.80	81.68	91.67	45.92	12.31	141.8
$M_g^u = M^u,\ M_p^u = 0$ and $M_g^T = M_p^T = M^T$										
1	300	251	98.00	99.98	99.98	100.0	99.28	97.66	77.45	123.9
2	500	402	92.01	98.38	100.9	100.3	96.78	94.60	56.93	110.3
4	900	704	72.44	93.63	101.1	96.89	93.48	70.98	3.306	31.18
6	1300	1006	36.91	87.77	101.0	89.01	99.56	52.87	1.984	25.50
8	1700	1308	32.73	85.34	95.78	82.69	100.7	48.14	1.057	19.77
12	2500	1776	31.88	84.32	93.97	80.77	101.3	46.12	0.441	12.77
16	3300	2244	31.03	83.99	93.70	80.21	102.1	45.10	0.406	12.17
20	4100	2644	30.86	83.82	93.10	79.59	102.1	44.78	0.373	11.40
24	4900	3044	30.37	84.07	93.56	79.69	102.0	45.30	0.374	11.34
32	6500	3844	29.31	82.66	90.46	76.90	102.0	43.54	0.369	11.10
$M_g^u = M_p^u = M^u$ and $M_g^T = M^T,\ M_p^T = 0$										
1	402	200	90.81	68.11	91.36	96.15	99.42	95.38	86.48	105.9
2	704	300	82.37	57.77	82.90	91.90	97.80	90.97	74.55	106.3
4	1308	500	45.43	40.88	32.78	53.70	80.07	71.81	14.16	142.4
6	1912	700	12.48	29.04	20.93	35.71	69.01	63.08	13.32	143.3
8	2516	900	7.990	21.90	12.90	25.77	69.64	61.46	12.36	143.4
12	3452	1300	6.163	17.55	9.528	20.61	65.62	56.87	12.25	142.2
16	4388	1700	3.989	16.40	8.771	18.66	66.02	54.52	12.26	142.1
20	5188	2100	3.692	15.82	8.873	17.36	68.14	48.12	12.28	142.0
24	5988	2500	3.255	15.99	8.274	16.95	64.84	46.52	12.30	141.9
32	7588	3300	2.283	12.90	7.604	16.74	59.34	43.95	12.31	141.8
$M_g^u = M_p^u = M^u$ and $M_g^T = M_p^T = M^T$										
1	402	251	90.81	68.11	90.19	102.7	98.54	88.17	77.45	123.9
2	704	402	82.37	57.77	77.77	99.16	95.03	80.46	56.93	110.3
4	1308	704	45.43	40.88	31.77	54.53	62.22	56.58	3.306	31.18
6	1912	1006	12.48	29.04	19.71	35.62	12.12	34.48	1.984	25.50
8	2516	1308	7.990	21.90	11.79	24.15	9.885	29.21	1.057	19.77
12	3452	1776	6.163	17.55	8.775	19.12	7.687	25.99	0.441	12.77
16	4388	2244	3.989	16.40	7.970	17.15	5.304	24.32	0.406	12.17
20	5188	2644	3.692	15.82	7.535	16.35	5.153	23.90	0.373	11.40
24	5988	3044	3.255	15.99	8.087	16.37	5.023	24.03	0.374	11.34
32	7588	3844	2.283	12.90	7.530	15.66	4.698	22.09	0.369	11.10

Table A5. Thermoelasticity problem. Case 2 (homogeneous boundary condition for elasticity and non-homogeneous boundary condition for temperature on perforations). Unstructured coarse grids. $M = M^u = M^T$. Relative L^2 and H^1 error in %. DOF_h = 170,460.

| M	DOF_H^u	DOF_H^T	Quasi-Structured				Unstructured			
			$e(u)_{L^2}$	$e(u)_{H^1}$	$e(T)_{L^2}$	$e(T)_{H^1}$	$e(u)_{L^2}$	$e(u)_{H^1}$	$e(T)_{L^2}$	$e(T)_{H^1}$
1	402	251	98.47	91.35	76.32	103.8	98.44	93.52	72.88	95.42
2	704	402	94.78	82.68	52.28	92.76	94.43	86.17	54.50	93.85
4	1308	704	72.68	64.89	6.404	37.24	79.52	73.01	15.27	53.38
6	1912	1006	51.18	54.39	3.044	32.04	62.35	63.75	7.285	37.87
8	2516	1308	21.07	36.85	1.496	22.45	46.90	55.00	3.408	30.38
12	3452	1776	13.06	31.33	0.877	18.19	21.52	39.67	1.495	23.10
16	4388	2244	8.606	27.89	0.667	16.36	12.78	32.80	0.941	20.06
20	5188	2644	6.745	26.25	0.543	15.19	8.371	29.68	0.667	18.02
24	5988	3044	5.701	25.20	0.462	14.47	6.383	28.10	0.500	16.17
32	7588	3844	4.834	24.01	0.395	13.68	4.941	26.57	0.384	14.81
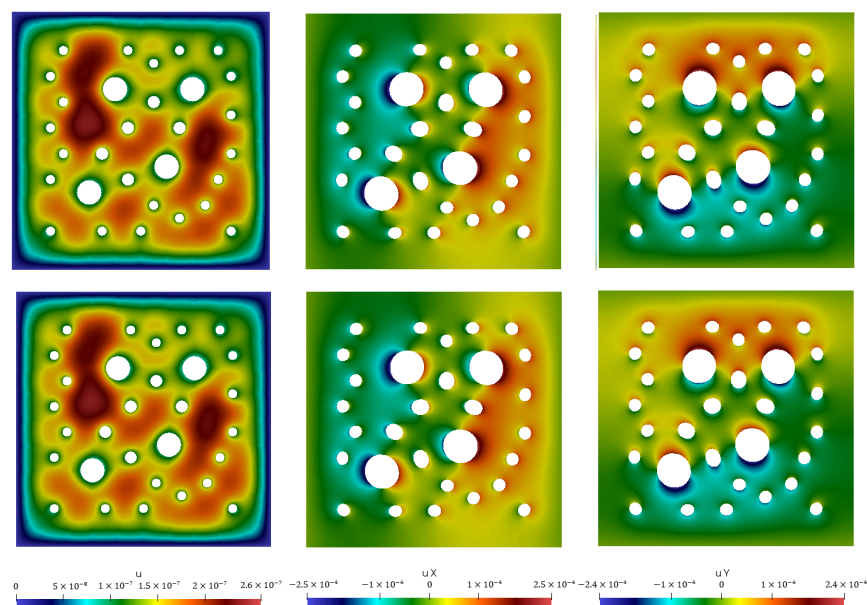
Figure A5. Thermoelasticity problem. Case 1 (non-homogeneous boundary condition for elasticity and homogeneous boundary condition for temperature on perforations). First column: temperature. Second column: displacement of X-component. Third column: displacement of Y-component. First row: Reference solution ($DOF_h = DOF_h^u + DOF_h^T$, with $DOF_h^u = 170,460$ and $DOF_h^T = 85,230$). Second row: Multiscale solution with 24 multiscale basis functions, $e(u)_{L^2} = 3.255$ and $e(T)_{L^2} = 8.087$ ($M_g^u = M_p^u = M_g^T = M_p^T = M$, $DOF_H = DOF_H^u + DOF_H^T$ with $DOF_H^u = 5988$ and $DOF_H^T = 3044$).

Case 1 with non-homogeneous boundary conditions for elasticity and homogeneous boundary conditions for temperature on perforations shows that, for displacement, we should use perforation boundary basis functions in order to approximate the non-homogeneous boundary condition for the elasticity part of the coupled system. For temperature, only outer boundary basis functions can be used because we have homogeneous boundary conditions for temperature. For Case 1 with $M_g^u = M_p^u = 24$, $M_g^T = 24$, and $M_p^T = 0$, we obtain a good results with 3% and 8% of L^2 errors for displacement and temperature, respectively. When we use only outer boundary basis functions for displacement ($M_p^u = 0$), we obtain a large error for both displacement and temperature. In Case 2 with homogeneous boundary conditions for elasticity and non-homogeneous boundary conditions for temperature on perforations, we can obtain good results with outer and perforation boundary basis functions for both displacement and temperature ($M_g^u = M_p^u = M^u$ and $M_g^T = M_p^T = M^T$). It should be noted that perforation boundary basis functions should be

added for displacement due to the coupled process for accurate multiscale approximation even for non-homogeneous boundary conditions for elasticity on perforations.
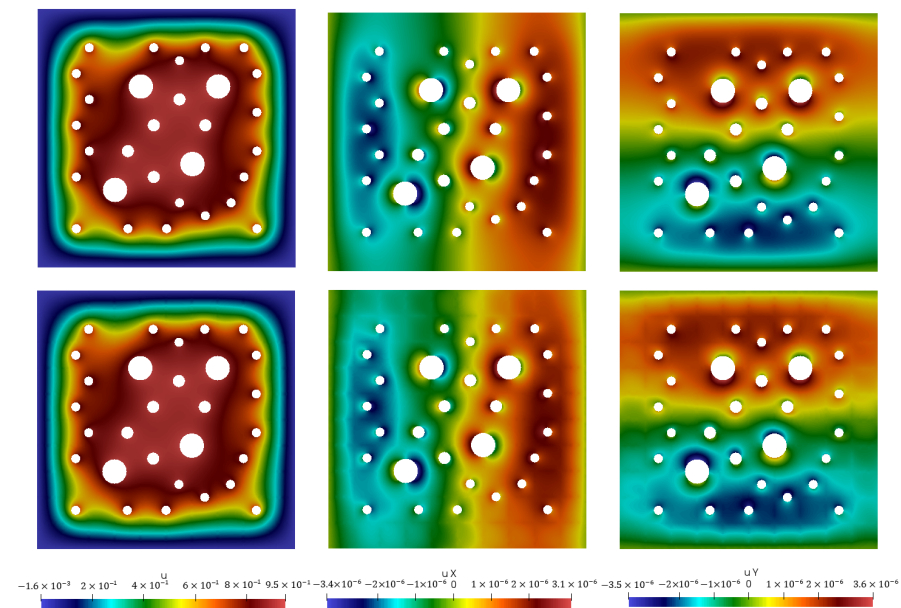

Figure A6. Thermoelasticity problem. Case 2 (homogeneous boundary condition for elasticity and non-homogeneous boundary condition for temperature on perforations). First column: temperature. Second column: displacement of X-component. Third column: displacement of Y-component. First row: Reference solution ($DOF_h = DOF_h^u + DOF_h^T$ with $DOF_h^u = 170{,}460$ and $DOF_h^T = 85{,}230$). Second row: Multiscale solution with 24 multiscale basis functions, $e(u)_{L^2} = 5.023\%$ and $e(T)_{L^2} = 0.374\%$ ($M_g^u = M_p^u = M_g^T = M_p^T = M = 24$, $DOF_H = DOF_H^u + DOF_H^T$ with $DOF_H^u = 5988$ and $DOF_H^T = 3044$).

References

1. Heinze, S. Wave solutions to reaction-diffusion systems in perforated domains. *Z. Anal. Und Ihre Anwendungen* **2001**, *20*, 661–676. [CrossRef]
2. Amaziane, B.; Goncharenko, M.; Pankratov, L. Homogenization of a convection–diffusion equation in perforated domains with a weak adsorption. *Z. Angew. Math. Und Phys.* **2007**, *58*, 592–611. [CrossRef]
3. Höhner, D.; Wirtz, S.; Scherer, V. A study on the influence of particle shape on the mechanical interactions of granular media in a hopper using the Discrete Element Method. *Powder Technol.* **2015**, *278*, 286–305. [CrossRef]
4. Sadeghi, R.; Shadloo, M.S.; Hopp-Hirschler, M.; Hadjadj, A.; Nieken, U. Three-dimensional lattice Boltzmann simulations of high density ratio two-phase flows in porous media. *Comput. Math. Appl.* **2018**, *75*, 2445–2465. [CrossRef]
5. Korneev, S.; Battiato, I. Sequential homogenization of reactive transport in polydisperse porous media. *Multiscale Model. Simul.* **2016**, *14*, 1301–1318. [CrossRef]
6. Iliev, O.; Lakdawala, Z.; Neßler, K.H.; Prill, T.; Vutov, Y.; Yang, Y.; Yao, J. On the pore-scale modeling and simulation of reactive transport in 3D geometries. *Math. Model. Anal.* **2017**, *22*, 671–694. [CrossRef]
7. Allaire, G.; Mikelić, A.; Piatnitski, A. Homogenization approach to the dispersion theory for reactive transport through porous media. *Siam J. Math. Anal.* **2010**, *42*, 125–144. [CrossRef]
8. Sánchez-Palencia, E. *Non-Homogeneous Media and Vibration Theory*; Lecture Notes in Physics; Springer: Berlin, Germany, 1980; Volume 127.
9. Bakhvalov, N.S.; Panasenko, G. *Homogenisation: Averaging Processes in Periodic Media: Mathematical Problems in the Mechanics of Composite Materials*; Springer Science & Business Media: Dordrecht, The Netherlands, 2012; Volume 36.
10. Allaire, G. Homogenization of the Navier-Stokes equations in open sets perforated with tiny holes II: Non-critical sizes of the holes for a volume distribution and a surface distribution of holes. *Arch. Ration. Mech. Anal.* **1991**, *113*, 261–298. [CrossRef]
11. Jing, W. A unified homogenization approach for the Dirichlet problem in perforated domains. *SIAM J. Math. Anal.* **2020**, *52*, 1192–1220. [CrossRef]
12. Vasilyeva, M.; Tyrylgin, A. Convolutional neural network for fast prediction of the effective properties of domains with random inclusions. *J. Phys.* **2019**, *1158*, 042034. [CrossRef]

13. Vasilyeva, M.; Tyrylgin, A. Machine learning for accelerating macroscopic parameters prediction for poroelasticity problem in stochastic media. *Comput. Math. Appl.* **2021**, *84*, 185–202. [CrossRef]
14. Efendiev, Y.; Hou, T.Y. *Multiscale Finite Element Methods: Theory and Applications*; Springer Science & Business Media: New York, NY, USA, 2009; Volume 4.
15. Hou, T.Y.; Wu, X.H. A multiscale finite element method for elliptic problems in composite materials and porous media. *J. Comput. Phys.* **1997**, *134*, 169–189. [CrossRef]
16. Muljadi, B.P.; Narski, J.; Lozinski, A.; Degond, P. Nonconforming multiscale finite element method for stokes flows in heterogeneous media. Part I: Methodologies and numerical experiments. *Multiscale Model. Simul.* **2015**, *13*, 1146–1172. [CrossRef]
17. Le Bris, C.; Legoll, F.; Lozinski, A. An MsFEM type approach for perforated domains. *Multiscale Model. Simul.* **2014**, *12*, 1046–1077. [CrossRef]
18. Henning, P.; Ohlberger, M. The heterogeneous multiscale finite element method for elliptic homogenization problems in perforated domains. *Numer. Math.* **2009**, *113*, 601–629. [CrossRef]
19. Chung, E.T.; Efendiev, Y.; Li, G.; Vasilyeva, M. Generalized multiscale finite element methods for problems in perforated heterogeneous domains. *Appl. Anal.* **2016**, *95*, 2254–2279. [CrossRef]
20. Chung, E.T.; Efendiev, Y.; Leung, W.T.; Vasilyeva, M.; Wang, Y. Online adaptive local multiscale model reduction for heterogeneous problems in perforated domains. *Appl. Anal.* **2017**, *96*, 2002–2031. [CrossRef]
21. Chung, E.T.; Leung, W.T.; Vasilyeva, M.; Wang, Y. Multiscale model reduction for transport and flow problems in perforated domains. *J. Comput. Appl. Math.* **2018**, *330*, 519–535. [CrossRef]
22. Chung, E.T.; Efendiev, Y.; Vasilyeva, M.; Wang, Y. A multiscale discontinuous Galerkin method in perforated domains. In Proceedings of the Institute of Mathematics and Mechanics, Maringá, Brazil, 22–23 September 2016; Volume 42, pp. 212–229.
23. Spiridonov, D.; Vasilyeva, M.; Leung, W.T. A Generalized Multiscale Finite Element Method (GMsFEM) for perforated domain flows with Robin boundary conditions. *J. Comput. Appl. Math.* **2019**, *357*, 319–328. [CrossRef]
24. Vasilyeva, M.; Chung, E.T.; Leung, W.T.; Wang, Y.; Spiridonov, D. Upscaling method for problems in perforated domains with non-homogeneous boundary conditions on perforations using Non-Local Multi-Continuum method (NLMC). *J. Comput. Appl. Math.* **2019**, *357*, 215–227. [CrossRef]
25. Zhao, L.; Chung, E.T. An analysis of the NLMC upscaling method for high contrast problems. *J. Comput. Appl. Math.* **2020**, *367*, 112480. [CrossRef]
26. Chung, E.T.; Efendiev, Y.; Leung, W.T. Constraint energy minimizing generalized multiscale finite element method. *Comput. Methods Appl. Mech. Eng.* **2018**, *339*, 298–319. [CrossRef]
27. Fu, S.; Chung, E.; Mai, T. Constraint energy minimizing generalized multiscale finite element method for nonlinear poroelasticity and elasticity. *J. Comput. Phys.* **2020**, *417*, 109569. [CrossRef]
28. Efendiev, Y.; Galvis, J.; Li, G.; Presho, M. Generalized multiscale finite element methods: Oversampling strategies. *Int. J. Multiscale Comput. Eng.* **2014**, *12*, 465–484 [CrossRef]
29. Henning, P.; Peterseim, D. Oversampling for the multiscale finite element method. *Multiscale Model. Simul.* **2013**, *11*, 1149–1175. [CrossRef]
30. Calo, V.M.; Efendiev, Y.; Galvis, J.; Li, G. Randomized oversampling for generalized multiscale finite element methods. *Multiscale Model. Simul.* **2016**, *14*, 482–501. [CrossRef]
31. Chung, E.T.; Efendiev, Y.; Leung, W.T. An online generalized multiscale discontinuous Galerkin method (GMsDGM) for flows in heterogeneous media. *arXiv* **2015**, arXiv:1504.04417.
32. Chung, E.T.; Efendiev, Y.; Leung, W.T. An adaptive generalized multiscale discontinuous Galerkin method for high-contrast flow problems. *Multiscale Model. Simul.* **2018**, *16*, 1227–1257. [CrossRef]
33. Geuzaine, C.; Remacle, J.F. Gmsh: A 3-D finite element mesh generator with built-in pre-and post-processing facilities. *Int. J. Numer. Methods Eng.* **2009**, *79*, 1309–1331. [CrossRef]
34. Logg, A.; Mardal, K.A.; Wells, G. *Automated Solution of Differential Equations by the Finite Element Method: The FEniCS Book*; Springer Science & Business Media: Berlin, Germany, 2012; Volume 84.